



Theory and modeling of relevance to prompt-NO formation at high pressure

Stephen J. Klippenstein^{a,*}, Mark Pfeifle^a, Ahren W. Jasper^a, Peter Glarborg^b

^aChemical Sciences and Engineering Division, Argonne National Laboratory, Argonne, IL 60439, USA

^bDepartment of Chemical and Biochemical Engineering, Technical University of Denmark, DK-2800 Kgs. Lyngby, Denmark



ARTICLE INFO

Article history:

Received 13 November 2017

Revised 2 March 2018

Accepted 2 April 2018

Available online 21 May 2018

Keywords:

Theoretical kinetics

Prompt NO

NO_x

High pressure

NCN kinetics

ABSTRACT

An improved understanding of NO_x formation at high pressures would be of considerable utility to efforts to develop advanced combustion devices. A combination of theoretical and modeling studies are implemented in an effort to improve the accuracy of models for the prompt NO process, which is the dominant source of NO under many conditions, and to improve our understanding of the role of this process at high pressures. The theoretical effort implements state-of-the-art treatments of NCN thermochemistry, the interrelated CH + N₂ and NCN + H kinetics, and the kinetics of the NCN + OH reaction. For both reaction systems, we implement high level ab initio transition state theory based master equation simulations paying particular attention to the role of stabilization processes. For the NCN + H kinetics we include a treatment of inter-system crossing. The modeling effort focuses on exploring the role of pressure and prompt NO for premixed laminar flames at pressures ranging from 1 to 15 atm, via a comparison with the available experimental data. Additional simulations at higher pressures further explore the mechanistic changes at the pressures of relevance to applied combustion devices (e.g., 100 atm).

© 2018 The Combustion Institute. Published by Elsevier Inc. All rights reserved.

1. Introduction

Combustion of natural gas is expected to account for a major share of future power and heat generation into the future, prompting ever more stringent legislation on its pollutant emissions, particularly for NO_x. Since natural gas contains no or negligible amounts of fuel-bound nitrogen, formation of NO arises from fixation of N₂ in the combustion air. It is particularly important to understand the details of the NO_x formation process at the high pressures of relevance to advanced combustion devices.

The prompt NO mechanism is the dominant source of NO in turbulent diffusion flames [1], which are the most common practical flame configuration. The mechanism is initiated by attack of CH_n-radicals on N₂ [2,3]. Early modeling studies [4,5] identified the reaction of CH with N₂ as the most important initiation step. This reaction was initially believed to form HCN + N [6], but subsequent theoretical work led to the realization that it instead proceeds via insertion of CH into the N₂ triple bond, yielding NCN + H [7,8]:



A sustained experimental and modeling effort by Lamoureux et al. [9–15] has extensively explored the role of NCN for prompt NO formation in low pressure flames. This work included the development of new experimental techniques for quantitatively measuring NCN [9,12], HCN [13,14], and CN [14] concentration profiles. Their complete set of measured flame profiles for NCN, CN, HCN, CH, NCO, and NO in CH₄ and C₂H₂ flames were used to develop a comprehensive chemical kinetic model [10,14,15] for prompt NO. The resulting model clearly illustrates the important role of NCN in the prompt NO mechanism.

Reliable predictions of prompt NO formation require an accurate rate constant for reaction R1, as well as the ability to predict the selectivity in the oxidation of NCN to form NO and N₂, respectively [16]. The value of *k*₁ is now fairly well established from experimental [17,18] and theoretical work [8,19,20]. A series of experimental studies by Friedrichs and coworkers who determined rate constants for several of the NCN reactions, i.e., NCN + M [21], NCN + H [22], NCN + O [21], NCN + O₂ [23], and NCN + NO [24] and corresponding theoretical studies by Lin and coworkers of NCN + H [20], NCN + O [25], NCN + OH [26], and NCN + O₂ [27] have greatly expanded our understanding of the kinetics of NCN reactions. Furthermore, Olzmann and coworkers have explored the collisional relaxation [28], thermal dissociation [29], and reaction with NO [30]. Nevertheless, important aspects of both the thermochemistry and reactions of NCN are still in discussion

* Corresponding author.

E-mail address: sjk@anl.gov (S.J. Klippenstein).

[15,22,31] and modeling predictions of prompt NO formation have a higher degree of uncertainty than desired [16].

Continuing advances in theoretical kinetics methodologies allow for ever more accurate predictions of elementary reaction kinetics and thermochemistry. Here we apply state-of-the-art methods to explore the thermochemistry of NCN, and the temperature and pressure dependent kinetics of the $\text{NCN} + \text{H}$ and $\text{NCN} + \text{OH}$ reactions. The thermochemistry of NCN is central to the prompt NO mechanism and has been the subject of considerable debate [15,22,31]. The high level electronic structure methods applied here reduce the uncertainty in the NCN heat of formation to about $0.2 \text{ kcal mol}^{-1}$. Although the important $\text{NCN} + \text{H}$ reaction has been studied both theoretically and experimentally [20,22], there is still some uncertainty in both the rates and branching. Of particular concern to the present study is the possible role of stabilization to HNCN at high pressures (e.g., 100 atm). Here ab initio transition state theory (TST) based master equation simulations are used to predict both the overall rates and the stabilization probability. As part of this analysis we explore the possible role of intersystem crossing on the kinetics of the $\text{NCN} + \text{H}$ reaction. The $\text{NCN} + \text{OH}$ reaction, which may be of relevance under lean ignition conditions, has only been studied theoretically [26]. Again, some stabilization of the NCNOH adduct is possible, and our advanced theoretical analyses should better delineate the possible role of this reaction. We also discover a significant additional reaction pathway for this reaction.

There is considerable uncertainty in the impact of pressure on prompt NO formation. Formation of nitric oxide has been studied at elevated pressure in premixed [32–40] and non-premixed [41–45] flames. The objective of the chemical kinetic modeling aspect of the present work is to explore the effect of pressure on prompt NO formation, through comparison of model predictions with these experimental observations as well as through predictions for even higher pressure conditions. The latter emphasize the high pressure conditions relevant for gas engines and gas turbines. As part of this modeling analysis we also explore the role of stabilization in the $\text{NCN} + \text{H}$ and $\text{NCN} + \text{OH}$ reactions.

2. Theory

2.1. Electronic structure

High accuracy kinetic descriptions rely on quantitative electronic energies for a range of molecular configurations. The most accurate descriptions of the latter are obtained through composite electronic structure techniques that employ a variety of methods to explore various aspects of the electronic interactions [46]. Furthermore, the most appropriate method depends to some extent on the particular molecular geometries of interest, with single-reference based methods being particularly useful for stable molecules, while multi-reference methods are often more effective in treating the more complex interactions that arise in the TS region [47].

For molecular geometries that are well described with single-reference wavefunctions, the CCSD(T) method (coupled cluster theory with treatment of singles, doubles, and perturbative triples electronic excitations) [48] provides a particularly effective treatment of the energies. Thus, most high accuracy calculations focus on the evaluation of the complete-basis set (CBS) limit for the CCSD(T) method. Separate calculations of other effects (e.g., higher order electronic excitations, core-valence interactions, ...) can then be combined to obtain high accuracy electronic energies [46]. For kinetics purposes, it is also important to have highly accurate estimates of the vibrational frequencies, with the CCSD(T) method again providing a particularly accurate means for predicting them.

In recent work, we have demonstrated the utility and accuracy of two specific composite methods, termed ANLO and ANL1,

through a detailed analysis of the various components as well as comparison with values from the Active Thermochemical Tables (ATcT) approach [49]. The ANLO method couples a CCSD(T)/cc-pVTZ rovibrational analysis with a CCSD(T)/CBS analysis based on explicit calculations for partially augmented cc-pVQZ and cc-pV5Z basis sets. Corrections for higher order excitations [CCSDT(Q)], core-valence interactions, vibrational anharmonicities, relativistic effects, diagonal Born-Oppenheimer effects, and spin-orbit coupling, are also included. The ANL1 method differs from the ANLO method in its use of larger basis sets, and thus more quantitative approach to the CBS limit. As part of this analysis [49], ANLO predictions of the heat of formation were obtained for 348 combustion relevant species. The comparison with ATcT values for 150 of these species indicates that, for species in which the multireference effects are not too large, the 2σ uncertainty in the predicted heat of formation is about $0.25 \text{ kcal mol}^{-1}$. Here we make extensive use of the ANLO and ANL1 approaches in exploring the potential energy surfaces for the NCN species, and the $\text{NCN} + \text{H}$ and $\text{NCN} + \text{OH}$ reactions.

For bond-fission TSs, multireference methods based on complete-active space (CAS) reference wavefunctions are particularly effective [47]. CASPT2 (which includes a second order perturbative treatment of the singles and double excitations from the CAS reference space) and multireference configuration interaction, MRCI, (which includes a full treatment of the single and doubles excitations) provide two alternative effective means for predicting the energies. For the latter approach, the Davidson correction [50] provides semiquantitative estimates for higher order excitations. Here, we employ both CASPT2 and Davidson corrected MRCI (MRCI+Q) in exploring the TS regions of the various bond fission reactions of relevance to the studied reactions.

The results obtained with CASPT2 and MRCI+Q methods are occasionally somewhat discordant. This discordancy can result in significant uncertainties in the predicted rate coefficients. Recently, we have demonstrated that using multireference methods to explore the splitting between electronic states can yield better consistency between the various methods [51]. This spin-splitting approach involves a coupling of the multireference evaluation of the spin-splitting with a higher order (e.g., CCSD(T) based) evaluation of the energy of the higher spin-state. This improved consistency is expected to correlate with higher accuracy and so this method is used here in our evaluation of the reactive flux for the bond-fission TSs.

2.2. Kinetics

The present theoretical kinetics predictions are based on a combination of ab initio TST [47,52], to predict the microcanonical and canonical partition functions, and the master equation [53,54] to explore the effects of collisional energy transfer on the pressure dependence of the kinetics. The master equation calculations employ exponential down models coupled with Lennard-Jones collision rates for the collisional energy transfer. The temperature dependence of the averaged downwards energy transfer was modeled as $A (T/298 \text{ K})^{0.85} \text{ cm}^{-1}$, in analogy with prior experimental and theoretical work [55–57]. For the HNCN and NCNOH systems the parameter A was taken to be 100 and 150 cm^{-1} , respectively. These values are taken from analogy with our master equation studies of similar sized oxygenated hydrocarbon molecules (e.g., CH_3OH , $\text{C}_2\text{H}_5\text{OH}$, CH_3CHO) where comparison with pressure dependent experimental data yielded fitted values. The uncertainty in these parameters likely contributes the most to the uncertainty in the final rate predictions, at least for pressures where the rate is predicted to deviate from the high-pressure and collisionless limits. The Lennard-Jones collision rates were estimated from crude comparisons with similar species.

Table 1
Vibrational frequencies in NCN.

Method	Basis	$\nu_{\text{bend}}^{\text{a}}$ cm ⁻¹	$\nu_{\text{sym stretch}}^{\text{a}}$ cm ⁻¹	$\nu_{\text{asym stretch}}^{\text{a}}$ cm ⁻¹	ZPE kcal/mol
Expt		423 (423)	1197 (1245)	1475 (1472)	
RR-CCSD(T)	cc-pVQZ	428	1029	4178	8.67
RU-CCSD(T)	cc-pVQZ	423	1187	2541	6.54
UU-CCSD(T)	cc-pVQZ	431	1253	1453	5.10
UU-CCSD(T)	cc-pVTZ	427	1245	1439	5.06
UU-CCSDT(Q)	cc-pVTZ	418	1229	1461	5.04
UU-MP2	cc-pVTZ	524	917	1361	4.76
CASPT2(6e,6o)	cc-pVQZ	424	1247	1537	5.19
MRCI+Q(6e,6o)	cc-pVTZ	427	1252	1518	5.18
MRCI+Q(14e,12o)	aug-cc-pVTZ	417	1229	1467	5.05
B3LYP	cc-pVTZ	449	1274	1561	5.34
B2PLYPD3	cc-pVTZ	460	1292	1425	5.20
B2PLYPD3;anh	cc-pVTZ	459	1265	1430	5.22
B2PLYPD3	cc-pVQZ	461	1292	1425	5.20
Best Theory ^b		423	1218	1486	5.13

^a The experimental values are the fundamental frequencies observed in the matrix isolation experiments of Jacox and coworkers [68,69] and in parentheses from the LIF experiments of Lamoureux and coworkers [12]. The theoretical frequencies are harmonic frequencies, except for the B2PLYP-D3;anh values, which are the fundamental frequencies predicted by second order vibrational perturbation theory. The MRCI+Q(14e,12o)/aug-cc-pvtz calculations were performed as part of the effort described in [70].

^b Theoretical result given by UU-CCSD(T)/CBS(TZ,QZ) + UU-CCSDT(Q)/cc-pVTZ - UU-CCSD(T)/cc-pVTZ + B2PLYP-D3/cc-pVTZ;anharmonic - B2PLYP-D3/cc-pVTZ;harmonic.

For reaction channels with well-defined barriers we perform conventional TST calculations, based on the ANL0/1 stationary point properties. The state counts are based on rigid-rotor harmonic oscillator (RRHO) assumptions coupled with one-dimensional hindered rotor treatments. Asymmetric Eckart tunneling corrections are also included.

For barrierless reactions, the TS lies at separations where single reference methods are inappropriate. Furthermore, in this region the transition from free rotor to bending motion for a number of the modes is not well captured by traditional RRHO state counting procedures. For these barrierless channels, we implement the variable reaction coordinate (VRC)-TST approach [58,59], which provides an effective treatment of the latter difficulty through Monte Carlo integration of the classical phase space representation of the partition function for the key low frequency modes. The requisite potential energies are evaluated through direct CASPT2 evaluations for each of the randomly sampled configurations. This direct CASPT2 VRC-TST approach commonly leads to rate constants with expected uncertainties of 20 to 30% [59,60].

2.3. Software

The present electronic structure calculations were performed with the MOLPRO [61], CFOUR, [62], MRCC [63], and Gaussian [64] software packages. The VRC-TST calculations were performed with the VaReCoF software [65]. The master equation calculations were performed with the MESS software [66]. The intersystem crossing calculations were performed with the NST software [67].

2.4. NCN thermochemistry

The thermodynamic properties for NCN are discussed in detail elsewhere [16]. There are two subtleties involved in the accurate theoretical treatment of the energetics and kinetics of the NCN radical. Both subtleties relate to the neglect or enforcement of spin conservation in the electronic wavefunction. Within CCSD(T) theory, a spin-restriction can be implemented at the Hartree Fock (HF) level and/or at the CCSD(T) level. Typically, such spin restrictions have at most modest effects on CCSD(T) calculated properties.

However, for NCN such spin restrictions strongly affect both the vibrational frequencies and the CBS limit of the CCSD(T) energy.

The results provided in Table 1 demonstrate the strong sensitivity of the CCSD(T) predictions for the asymmetric stretch vibrational frequency. With both the RR-CCSD(T) (where both the HF and the CCSD(T) wavefunctions are spin-restricted) and RU-CCSD(T) methods (where the HF is spin-restricted, while the CCSD(T) is not) the predicted frequency is more than 1000 cm⁻¹ too large. These shortcomings map into errors in the predicted vibrational zero-point energy (ZPE) of 3.5 and 1.4 kcal/mol, respectively. They arise from symmetry breaking problems, where small displacements from the symmetrical NCN geometry result in aphysical variations in the wavefunctions. Unrestricted wavefunctions often bypass these difficulties and here the UU-CCSD(T) predictions (where neither the HF nor the CCSD(T) wavefunctions are spin restricted) are in reasonably good agreement with experiment, with a maximum discrepancy of 56 cm⁻¹ at the UU-CCSD(T)/cc-pVQZ level.

Notably, the inclusion of quadruple excitations (i.e., with the UU-CCSDT(Q)/cc-pVTZ method) improves the agreement for each of the modes. Furthermore, there is reasonably good agreement between the UU-CCSD(T) predictions and multireference methods where such symmetry breaking issues are absent by construction. These multireference calculations employ a 6 electron 6 orbital (6e,6o) active space consisting of the π -space of NCN or a full valence (14e,12o) active space. The good consistency amongst the present multireference calculations is encouraging. Oddly there is a significant discrepancy with our earlier [19] CASPT2(6e,6o) calculations, perhaps due to differences in the internal contractions. Interestingly, the B2PLYP-D3 density functional method also performs quite well, which suggests the appropriateness of this method for exploring the effect of anharmonicities. A best theoretical result, obtained by combining the UU-CCSD(T) complete basis set (CBS) limit (obtained from an extrapolation of the cc-pVTZ and cc-pVQZ results) with the difference between the UU-CCSDT(Q) and UU-CCSD(T) results (for the cc-pVTZ basis), and the difference between the anharmonic and harmonic evaluations for the B2PLYP-D3 methods (again for the cc-pVTZ basis), agrees with experiment to within 21 cm⁻¹, which themselves may be slightly perturbed by their determination in a matrix.

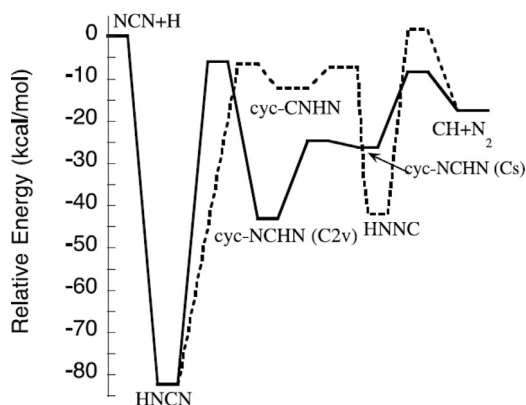


Fig. 1. Schematic plot of the ANL1 stationary points on the doublet potential energy surface for the NCN + H and CH + N₂ reactions. The solid line denotes the dominant pathway, while the dashed line denotes a secondary pathway that may be of minor importance at the high energies of the NCN + H reactants.

The spin contamination in NCN wavefunctions also presents considerable ambiguities in the CCSD(T)/CBS energy limit. In particular, RU- and RR-CCSD(T)/CBS predictions for the NCN 0 K heat of formation (evaluated relative to H₂, CH₄, and N₂ references from v1.122b of the ATcT) differ by 1.01 kcal/mol, with the UU-CCSD(T) predicted heat of formation falling between the two. The inclusion of quadruple excitations, through the CCSDT(Q) approach, generally ameliorates such spin treatment dependencies. For this case, appending a UU-CCSDT(Q)/cc-pVDZ correction (as in the ANL0 method [49]) reduces the discrepancy to 0.22 kcal/mol. Meanwhile, incorporating a CCSDTQ(P)/cc-pVDZ correction and extending the CCSDT(Q) correction to the cc-pVTZ basis (as in the ANL1 method [49]) reduces the discrepancy to 0.04 kcal/mol.

As discussed above, the ANL0 and ANL1 methods also include further corrections for core-valence interactions, vibrational anharmonicities, relativistic effects, and diagonal Born-Oppenheimer effects. For the ANL0 method these corrections are 0.78, 0.82, -0.39, and 0.12 kcal/mol when evaluated relative to H₂, CH₄, and NH₃ as references. The final ANL0 and ANL1 predictions of 107.66 and 107.61 kcal/mol for the 0 K heat of formation are in excellent agreement with the ATcT value of 107.65 kcal/mol [16]. Notably, the 298 K ATcT value is 1.5 kcal/mol higher than the value employed in the most recent modeling study of Lamoureux et al. [15]. This discrepancy is well outside the expected uncertainty of 0.2–0.3 kcal/mol in the theoretical predictions.

2.5. The NCN + H reaction

2.5.1. Methodology – potential energy surface

The NCN + H reaction can occur via either doublet or quartet electronic states. On the doublet surface, this reaction is closely related to the reverse reaction of CH with N₂ (cf. Fig. 1). The present theoretical treatment of the kinetics on the doublet surface makes only minor modifications to our prior detailed analysis of the CH + N₂ reaction [19]. In particular, we employ the ANL1 method [49] to obtain higher accuracy thermochemical estimates for each of the stationary points (cf. Table 2). This update for the doublet surface most strongly affects the enthalpy of NCN, due to spin-conservation and symmetry breaking issues, as discussed above. Symmetry breaking issues also arise in the cyc-NCHN vibrational analysis, which are again solved by employing the UU-CCSD(T) method.

The TS connecting cyc-NCHN (C_{2v}) with HNCN is not well treated with single reference methods. Thus, the present analysis employs the multireference properties (i.e., the CAS+1+2+QC(11e,11o)/aug-cc-pVQZ//CASPT2(11e,11o)/aug-cc-pVTZ energy

Table 2

Stationary point energies (kcal/mol) on doublet potential energy surface for NCN + H and CH + N₂.^a

Species	CCSD(T)/CBS// B3LYP/6-311++ G(3df,2p) ^b	CCSD(T)/CBS// CASPT2/ATZ ^c	ANL1
NCN + H	0	0	0
HNCN	-82.99	-83.10	-82.30
cyc-NCHN (C _{2v})	-43.20	-43.86	-43.11
cyc-NCHN (C _s)	-28.00	-27.88	-26.22
cyc-CNHN	-13.35	-13.19	-12.18
HNNC	-43.60	-43.22	-41.96
HNCN = cyc-NCHN (C _{2v})	-8.81	-8.54 ^d	-5.95 ^d
cyc-NCHN (C _{2v}) = cyc-NCHN (C _s)	-24.86	-24.03	-23.88
cyc-NCHN = CH+N ₂	-8.82	-8.66	-8.47
HNCN = cyc-CNHN	-7.68	-7.08	-6.47
cyc-CNHN = HNNC	-4.58	-8.73	-7.33
HNNC = CH + N ₂	0.66	-0.04	1.66
CH+N ₂	-19.54	-19.54	-17.74

^a Includes ZPE corrections.

^b From [20].

^c From [19].

^d These values are derived from the multireference calculations of Harding et al. [19]. They are based on multireference estimates of the TS energy relative to various reference geometries. The ANL1 value is different due to changes in the energies of those references.

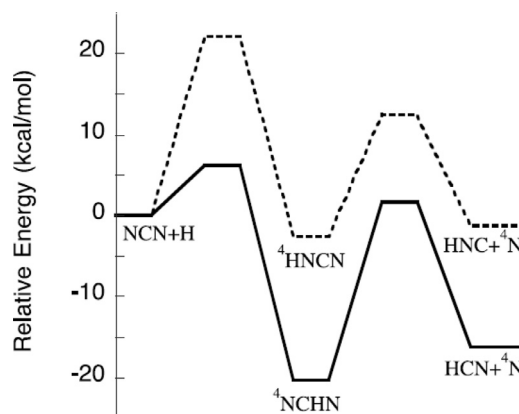


Fig. 2. Schematic plot of the ANL1 stationary points on the quartet potential energy surface for NCN + H. The solid line denotes the pathway arising from addition to the C atom, while the dashed line denotes the pathway arising from addition to one of the N atoms.

and the CASPT2(11e,11o)/aug-cc-pVTZ rovibrational properties) from Harding et al. [19]. There the energies were evaluated relative to three separate references: CH + N₂, cyc-NCHN (C_{2v}), and ⁴NCHN. The new ANL1 energies for these reference species are somewhat different from those employed in [19]. Employing the ANL1 reference energies results in an average zero-point-corrected TS energy of -6.0 kcal/mol relative to NCN + H. Interestingly, direct application of the ANL1 method to this TS yields either -5.5 or -4.1 kcal/mol, depending on which of two HF solutions are employed, with the lower value correlating with the solution with the smaller T1 diagnostic. It is reassuring that the multireference and higher order coupled cluster based results are reasonably consistent.

The reaction on the quartet state (cf. Fig. 2) was recently studied by Teng et al. [20]. We have updated their analysis with ANL1 predictions for the energetics (cf. Table 3) and rovibrational properties of the stationary points. The TS from NCN + H to ⁴NCHN suffers from spin-contamination and symmetry breaking problems in much the same way that NCN does. Again, these issues are most severe for the vibrational analysis. A UU-CCSD(T) based vibrational

Table 3Stationary point energies (kcal/mol) on NCN + H quartet potential energy surface^a

Species	CCSD(T)/CBS// B3LYP/6-311++ G(3df,2p) ^b	CCSD(T)/CBS// CASPT2/ATZ ^c	ANL1
NCN + H	0	0	0
NCHN	−21.26	−20.20	−20.30
HNCN	−3.49		−3.53
NCN + H = NCHN	5.51		6.25
NCHN = HCN + N	0.10		1.63
NCN + H = NHCN	22.60		22.15
NHCN = HNC + ⁴ N	9.56		12.39
NCHN = NHCN			30.40
HCN + N	−17.14	−17.37	−16.20
HNC + N	−3.55		−1.30

^a Includes ZPE corrections.^b From [20].^c From [19].

analysis, provides a result that appears reliable, agreeing reasonably well with B2PLYP-D3 and B3LYP vibrational analyses.

2.5.2. Methodology – intersystem crossing

Intersystem crossing (ISC) between the doublet and quartet surfaces may have some effect on the kinetics of the CHN₂ system. Here we are particularly interested in possible crossings in the neighborhood of the ⁴NCHN and ⁴HNCN minima. For the ⁴HNCN structure, we consider two limiting cases, no ISC and rapid ISC, and perform explicit calculations. For the ⁴NCHN structure, ISC was previously found to be the dominant bottleneck to reaction from CH + N₂ to HCN + N [7]. As a result, the reaction instead produces predominantly NCN + H. Furthermore, from the cyc-²NCHN structure, at energies exceeding the NCN + H asymptote, dissociation to CH + N₂ is rapid, suggesting that ISC from this structure is also not important for reaction on the doublet H + NCN PES. Finally, the barrier for dissociation to HCN + ⁴N from ⁴NCHN lies below the quartet entrance barrier for forming ⁴NCHN, again suggesting that ISC in the neighborhood of ⁴NCHN is unlikely to be significant. Thus, for simplicity, we assume that the rate of this process is negligible.

To estimate the ISC rate between ²HNCN and ⁴HNCN, non-adiabatic statistical theory [71–73] (NST) often called non-adiabatic TST or NA TST has been applied. For this purpose, minima on the seams of crossing (MSXs) between the lowest quartet state (1 ⁴A'') and the doublet ground state (1 ²A'') as well as the first excited doublet state (1 ²A') have been located. In the following, MSX1 denotes the ²A''/⁴A'' crossing, and MSX2 the ²A'/⁴A'' crossing. Geometry optimizations were carried out at the MRCI+Q(7e,6o)/def2-TZVP level of theory. The active space includes three out-of-plane π orbitals of the NCN fragment and three in-plane orbitals that have mostly N and C p-orbital character. CASSCF references without state averaging have been used in the geometry optimizations. The MRCI+Q calculations were internally contracted as implemented in Molpro [74–76] and relaxed-reference Davidson corrections [50] were applied. Geometry optimizations were carried out with the NST program [67], coupled with Molpro 2012 [61]. This code also performs a Koga-Morokuma frequency analysis [77] of the MSX, and calculates its RRHO density of states. The latter is convolved with a one-dimensional transition probability to obtain the effective number of states of the MSX that can be used to calculate microcanonical rate coefficients in the spirit of TST. These number of states are then directly incorporated in the MESS master equation solver.

For the transition probabilities, the double passage Landau–Zener and “weak coupling” [78] (denoted WC here) models have been used. For the rapid ISC and no ISC models, we presume the

transition probabilities are 1 and 0, respectively. Spin-orbit coupling matrix elements H_{SO} at the MSX structures were obtained with the full Breit–Pauli operator at the MRCI(13e,12o)/cc-pVTZ level in Molpro. This active space is obtained from the (7e,6o) space by adding the three σ/σ^* orbital pairs of the N–H and two N–C bonds. For MSX1, due to symmetry restrictions, only coupling elements between $|^2A'', S_z = \pm 1/2\rangle$ and $|^4A'', S_z = \pm 1/2\rangle$ are non-zero. For MSX2, the state pairs $|^12A', S_z = \pm 1/2\rangle$ and $|^14A'', S_z = \pm 3/2\rangle$ ($H_{SO,a}$), as well as $|^12A', S_z = \pm 1/2\rangle$ and $|^14A'', S_z = \mp 1/2\rangle$ ($H_{SO,b}$) give rise to non-vanishing coupling elements. According to the Wigner-Eckart theorem, $|H_{SO,a}|/|H_{SO,b}| = \sqrt{3}$. This can be accounted for by setting $|H_{SO}| = |H_{SO,a}|$ and $q_{el}=8/3$ for MSX2 in the rate calculations (see also the discussion in [7]). In the discussion below, only the larger matrix element $|H_{SO,a}|$ will be reported for MSX2. For MSX1, $q_{el}=2$ is used in combination with the non-zero matrix element. In doing so, the corresponding factors $q_{el}=2$ and $q_{el}=4$ are also taken into account when determining the density of states of the doublet and quartet wells.

MSX1 and MSX2 are structurally closer to the ⁴A'' equilibrium geometry than to the doublet minima. The ²A'' ground state has a nearly linear NCN substructure (174°) with an angled N–H bond (110°), while HNCN(²A') is perfectly linear in its equilibrium configuration. The NCN group in HNCN(⁴A'') on the other hand is significantly bent, giving rise to distinct trans and cis conformers. N–C–N angles of 116° (trans) and 121° (cis) were obtained at the MRCI+Q(7e,6o)/def2-TZVP level. Similarly, for the MSXs N–C–N angles of 107° (MSX1, trans), 114° (MSX1, cis), 115° (MSX2, trans), and 119° (MSX2, cis) have been found. The trans forms are more stable than the cis forms, in the case of HNCN(⁴A'') by 1.8 kcal mol^{−1}. A 8.6 kcal mol^{−1} isomerization barrier was found, and the harmonic frequencies corresponding to the torsion are 687 cm^{−1} (trans) and 705 cm^{−1} (cis) at the minima. Similarly, torsional frequencies in the range 699–855 cm^{−1} have been found for the cis and trans isomers of MSX1 and MSX2. Therefore, the conformers should be reasonably well described as separate species in the harmonic oscillator approximation. The zero-point corrected energies relative to trans-HNCN(⁴A'') are +2.5 (MSX1, trans), +3.0 (MSX1, cis), −1.2 (MSX2, trans), and +0.7 kcal mol^{−1} (MSX2, cis).

The spin-orbit coupling elements differ significantly between the trans and cis forms, especially for MSX2: Values of 11.2 (MSX1, trans), 13.0 (MSX1, cis), 6.4 (MSX2, trans), and 13.7 cm^{−1} (MSX2, cis) were obtained. Therefore ISC via the cis configuration is more likely than via the trans isomer. Both MSX1 and MSX2 (trans and cis) were implemented in the master equation as reaction channels between ⁴HNCN and ²HNCN, neglecting the distinction between ²A' and ²A''. The two doublet states are a Renner–Teller (² Π) pair that is degenerate at the linear geometry. This configuration is only 18.2 kcal mol^{−1} above the ²A'' minimum, compared with the HNCN well depth of more than 80 kcal mol^{−1}. A rapid interconversion between the doublet states is therefore very likely.

2.5.3. Methodology – kinetics

The master equation analysis considers the coupled doublet/quartet kinetics for the NCN + H and CH + N₂ bimolecular reactions as well as the stabilization/decomposition of HNCN. The underlying ab initio TST analyses of the microcanonical kinetics employs the ANL1 determined CCSD(T)/CBS rovibrational properties and stationary point energies for all but the NCN + H addition channel on the doublet surface. For that channel, we employ the variable reaction coordinate TST analysis from Harding et al. [19], but with updated UU-CCSD(T) based vibrational frequencies for NCN and with new direct CASPT2/cc-pVTZ energies. Modified Arrhenius representations for all the NCN + H and NCN + OH rate constants discussed here are provided in the supplementary material.

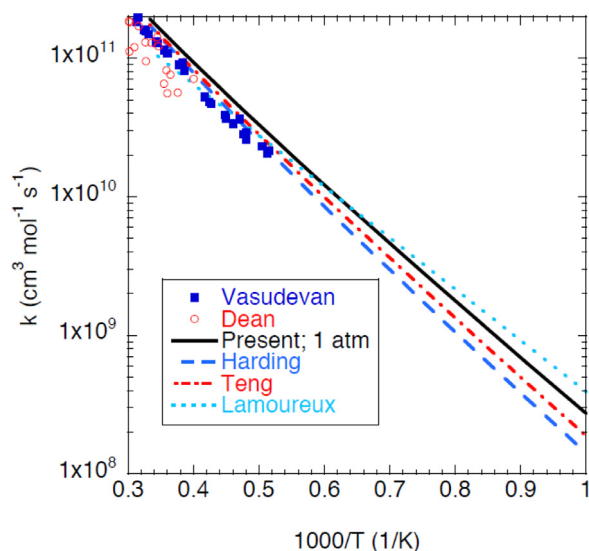


Fig. 3. Plot of the temperature dependence of theoretically predicted and experimentally observed rate constants for $\text{CH} + \text{N}_2$. Data are obtained from Dean et al. [17], Vasudevan et al. [18], Harding et al. [19], Teng et al. [20] and Lamoureux et al. [15].

2.5.4. Results and discussion

The ANL1 energies reported in Table 2 are reasonably consistent with the CCSD(T)/CBS values reported in our prior study. The most significant difference is the 1.8 kcal/mol decrease in the $\text{CH} + \text{N}_2$ exothermicity, which has important ramifications for the low temperature rate constant for $\text{CH} + \text{N}_2 \rightarrow \text{NCN} + \text{H}$. The other key difference is the 2.5 kcal/mol increase in the barrier for the conversion from cyc-NCHN (C_{2v}) to HNCN, which is the dominant bottleneck to reaction at high temperature. The net result is that our predictions for the collisionless limit of the $\text{CH} + \text{N}_2 \rightarrow \text{NCN} + \text{H}$ rate constant are increased slightly at lower temperature (e.g., by a factor of 2.1 at 1000 K), but are nearly identical at higher temperature (i.e., they are within a factor of 1.2–1.3 from 2000 to 3000 K) as illustrated in Fig. 3. Since direct experimental data are only available for high temperatures, there is little change in the comparison with experiment. Indeed, the theoretical predictions are still within the error bars of the direct measurements. It is interesting to note that the most recent optimized modeling value of Lamoureux et al. [15] is nearly identical to the current predictions near 1600 K, but has a smaller activation energy, apparently due to their use of a 1.5 kcal/mol lower enthalpy of formation for NCN. This leads to a result that varies from 40% too high (relative to our predictions) near 1000 K to 40% too low at 3000 K.

As shown in Fig. 4, at low temperatures the intersystem crossing from $^2\text{HNCN}$ to $^4\text{HNCN}$ dramatically increases the overall rate to form $\text{HNC} + ^4\text{N}$ from $\text{NCN} + \text{H}$. This increase occurs because the ISC process bypasses the high energy entrance barrier to form $^4\text{HNCN}$. At higher temperatures, the contribution from ISC gradually diminishes as the rate of decomposition of the $^2\text{HNCN}$ complex increases and as the rate of proceeding over the entrance barrier increases. By 1500 K, the ISC effect is negligible. Although not shown, the predictions based on the Landau-Zener model are essentially identical to those for the weak-coupling (WC) model. We note also that the treatment of ISC for HNCN has little effect on the predictions for $\text{CH} + \text{N}_2$.

The $\text{NCN} + \text{H}$ reaction has been studied experimentally by Faßheber et al. [22] who measured the total rate constant over the 962 to 2425 K range, and by Vasudevan et al. [18] who measured the decay of NCN over the 2378 to 2492 K range and then used their model for the $\text{CH} + \text{N}_2 \rightleftharpoons \text{H} + \text{NCN}$ reaction system to con-

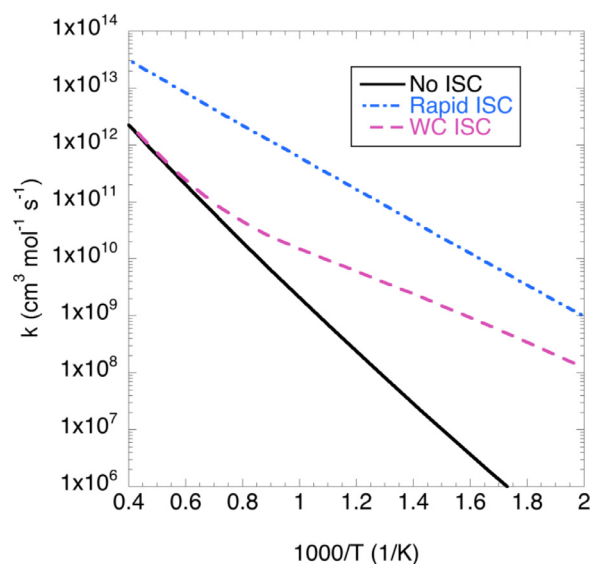


Fig. 4. Plot of the temperature dependence of the calculated rate constant for $\text{NCN} + \text{H} \rightarrow \text{HNC} + ^4\text{N}$ employing various models for the rate of intersystem crossing from $^2\text{HNCN}$ to $^4\text{HNCN}$.

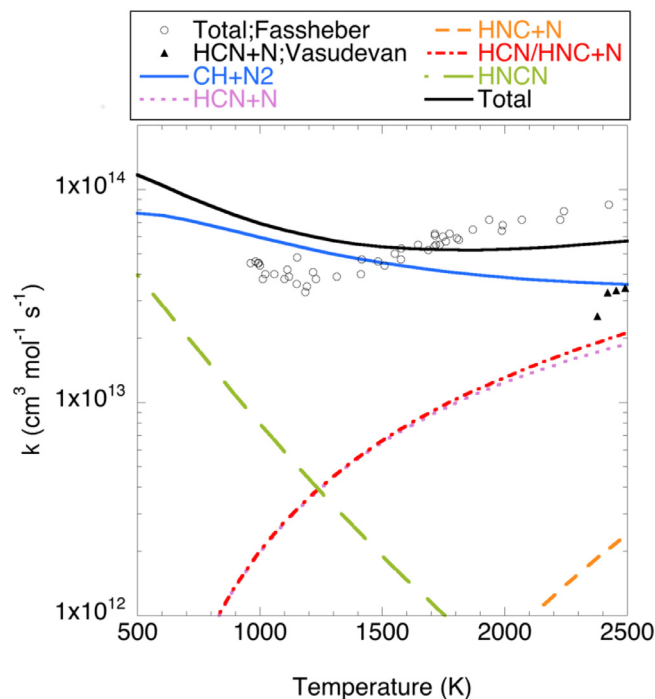


Fig. 5. Plot of the temperature dependence of theoretically predicted and experimentally observed rate constants for $\text{NCN} + \text{H}$. The theoretical results are for a pressure of 1 bar, while the experimental observations are for either a modest pressure range centered about that pressure [22] or for 0.4 bar [18].

vert this data to $\text{H} + \text{NCN} \rightarrow \text{HCN} + \text{N}$ rate constants. The latter analysis appears to have presumed that $\text{HCN} + \text{N}$ are the only products besides $\text{CH} + \text{N}_2$, whereas the present analysis suggests that $\text{HNC} + \text{N}$ may also be of some significance. Thus, for comparison purposes we consider the sum of the predicted rate constants to produce N along with its two different coproducts, HCN and HNC.

The present predictions for the temperature dependence of the $\text{H} + \text{NCN}$ reaction kinetics are illustrated in Fig. 5. The predicted pressure dependence is quite weak at the temperatures of relevance to the experimental observations. Thus, we restrict

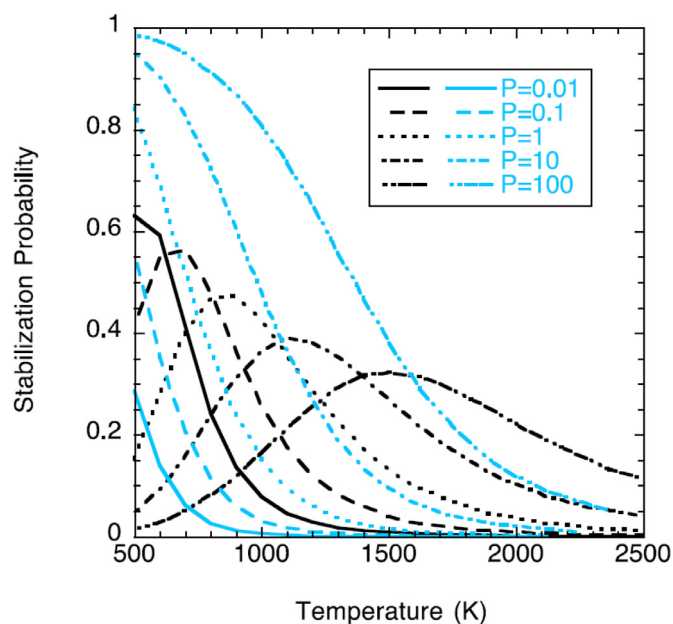


Fig. 6. Plot of the predicted temperature dependence of the probability of stabilization to HNCN (black lines) and cyc-NCHN (blue lines) in the $\text{CH} + \text{N}_2$ reaction for pressures ranging from 0.01 to 100 atm.

our attention in this comparison to a pressure of 1 bar, which is representative of the modest range explored experimentally. The present predictions are seen to be in reasonable agreement with the experimental results, with maximum discrepancies ($\sim 30\%$) for the total rate constant that are no larger than the experimental uncertainties. The predicted branching to the ^4N channels appears to be about a factor of two too small, but the experimental results for this channel are fairly indirect [18]. Assuming rapid ISC would improve the agreement for both the total rate and the branching, but the present calculations indicate that this presumption is unwarranted.

Importantly, the low temperature (i.e., near 1000 K) rate constant for the $\text{H} + \text{NCN}$ reaction places stringent constraints on the rate constant for the reverse $\text{CH} + \text{N}_2$ reaction in that same temperature range [15,22]. The reasonable agreement between theory and experiment for the $\text{H} + \text{NCN}$ reaction in this temperature range provides strong validation for our understanding of this key temperature range. The apparent modest overestimate (20 to 30%) in the theoretical predictions suggests that either the VRC-TST predictions for the $\text{H} + \text{NCN}$ high-pressure recombination rate are slightly too large, or the predictions for the bottleneck from HNCN to cyc-NCHN (C_{2v}) are not constraining enough. Reducing the stabilization probability would also slightly improve the agreement. However, since the agreement is within the errors bars of the experiment, no adjustments are made to the theoretical predictions.

The theoretical predictions of Teng et al. [20] are qualitatively similar to the present ones, but differ significantly in detail. For 1 bar pressure, they predict a total rate constant that is about 1.5 times larger. Their rate constant to form $\text{HCN} + \text{N}$ agrees quantitatively with the data of Vasudevan et al. [18]. Finally, their stabilization branching at low temperature is larger than predicted here, but then falls off more rapidly with increasing temperature.

At higher pressures for the $\text{CH} + \text{N}_2$ reaction stabilization to intermediate wells becomes quite significant, as illustrated in Fig. 6. At lower temperatures stabilization occurs to a weakly bound doublet adduct [6]. As shown by Lamoureux et al. [10], this complex is of no significance to prompt NO formation due to its weak binding energy. Notably, stabilization in the deep HNCN well (~ 82 kcal/mol relative to $\text{H} + \text{NCN}$) becomes quite probable, at least for

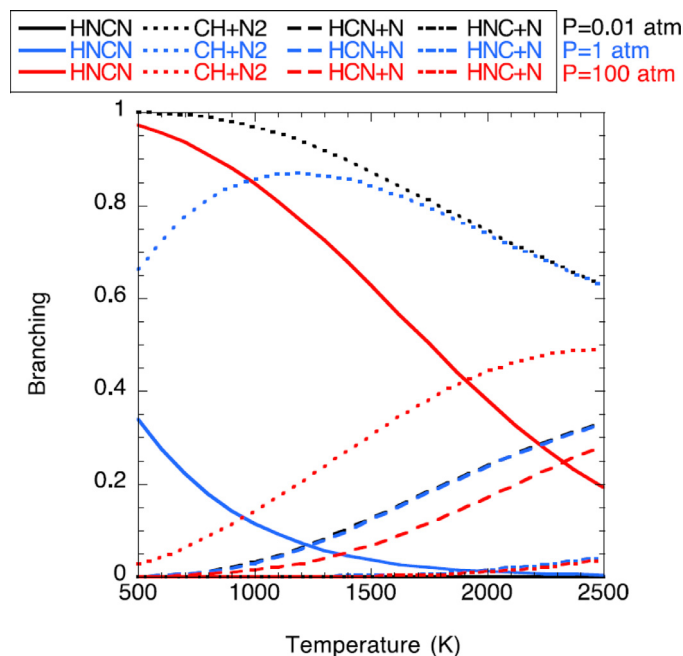


Fig. 7. Plot of the predicted temperature dependence of the branching in the $\text{H} + \text{NCN}$ reaction for pressures of 0.01, 1, and 100 atm. For $\text{HCN} + \text{N}$ and $\text{HNC} + \text{N}$ the $P = 0.01$ and 1 atm lines are overlapping. Note that the black solid line is very close to 0 for all temperatures.

not too high a temperature. This stabilization to HNCN is likely to be significant to the overall NO_x formation kinetics, as the HNCN species is stable enough to act as a sink for some of the $\text{CH} + \text{N}_2$ flux up until quite high temperature. At even higher pressures, stabilization to the cyc-NCHN well also becomes significant, especially at lower temperatures, where it even becomes the dominant process. Notably, at 100 atm stabilization dominates the kinetics up to about 1500 K. Meanwhile, at 1000 K, stabilization to HNCN is already significant (more than 10%) by 0.02 atm.

The corresponding temperature and pressure dependence of the branching in the $\text{H} + \text{NCN}$ reaction is illustrated in Fig. 7. In this case, the stabilization probability is considerably smaller because of the chemical activation energy present in the initial formation of the HNCN adduct. Nevertheless, at 100 atm, stabilization still dominates the kinetics for temperatures up to about 1500 K.

2.6. NCN + OH

2.6.1. Methodology

The kinetics of this reaction was studied in detail by Zhu et al. with ab initio TST based master equation methods [26]. We build from this work with (i) higher level evaluations of the potential energy surface, including the discovery of a new reaction pathway that dominates the kinetics, (ii) application of more advanced TS treatments, particularly for the barrierless channels, and (iii) a multiple well master equation treatment of the temperature and pressure dependent kinetics.

The stationary points on the potential energy surface were explored at the ANLO level [49] (cf. Fig. 8 and Table 4). Notably, the present ANLO predictions for the stationary point energies (relative to $\text{NCN} + \text{OH}$) deviate from the G2M(CC1) predictions of Zhu et al. by as much as 7 kcal/mol, while the average deviation is 3.8 kcal/mol. The consistent underestimate for the G2M predictions suggests that this method overestimates the energy of the reference NCN species.

Both the $\text{NCN} + \text{OH}$ entrance channel and the decomposition of NCONH to $\text{NCO} + ^3\text{NH}$ are radical-radical reactions. Such reactions

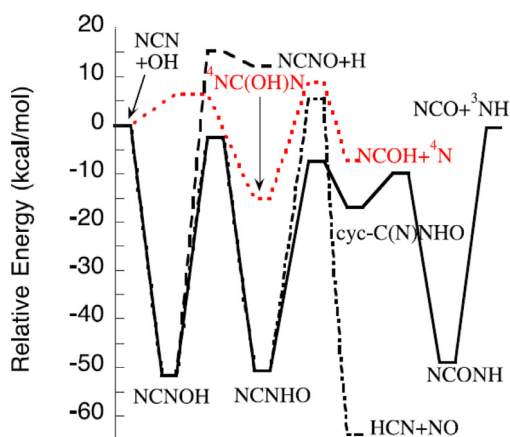


Fig. 8. Schematic plot of the kinetically relevant stationary points on the potential energy surface for NCN reacting with OH. The energies are zero-point corrected ANL0 values.

Table 4

Stationary point energies (kcal/mol) for the reaction of NCN with OH.

Species	ANL0	G2M(CC1) ^a
³ NCN + OH	0	0
NCO + ³ NH	-0.52	
NCNO + H	12.07	7.8
HCN + NO	-64.04	-66.9
NCOH + ⁴ N	-7.33	
NCNOH	-51.82	-53.3
NCNHO	-50.73	-52.9
cyc-C(N)NHO	-16.90	
NCONH	-48.98	
TS; NCNOH = NCNHO	-2.58	-4.5
TS; NCNHO = cyc-C(N)NHO	-7.61	
TS; cyc-C(N)NHO = NCONH	-10.03	
TS; NCNOH = H + NCNO	15.24	7.8
TS; NCNHO = HCN + NO	5.46	4.0
TS; NCN + OH = ⁴ NC(OH)N	6.30	
TS; ⁴ NC(OH)N = NCOH + ⁴ N	8.94	

^a From Zhu et al. [26].

are effectively barrierless (when considered in the association direction), with only a low energy submerged barrier (below the asymptotic energy of the fragments) correlating to the reorientation from a long-range van der Waals complex to that required for chemical bonding. As such, they require a careful consideration of variational and anharmonic effects and we implement the VRC-TST approach [79] for the analysis of their reactive flux.

For the two cases of interest here, the presence of resonance stabilization in the reacting fragments (NCN and NCO), which must be broken prior to chemical bond formation, also contributes to modest but still submerged barriers. The presence of an orbital degeneracy for one of the radicals in each reaction (OH and NCO both have $^2\Pi_{1/2}$ and $^2\Pi_{3/2}$ states that are split by only the spin-orbit splitting) further complicates the analysis. Calculations along the minimum energy paths indicate reasonable consistency between CASPT2 and MRCI+Q predictions with a maximum discrepancy of 18% in the energies along the minimum energy path for the NCN + OH case. For both cases, the discrepancies are reduced by about a factor of two when a spin-splitting based analysis is employed [51]. In each case we find that the inclusion of an IPEA (ionization potential - electron affinity) shift for CASPT2 yields dissociation curves that are intermediate between the MRCI+Q and regular CASPT2 results. Furthermore, they are in the best agreement with the values obtained with the spin-splitting considerations. Thus, our final analyses employ an IPEA shifted CASPT2 analysis.

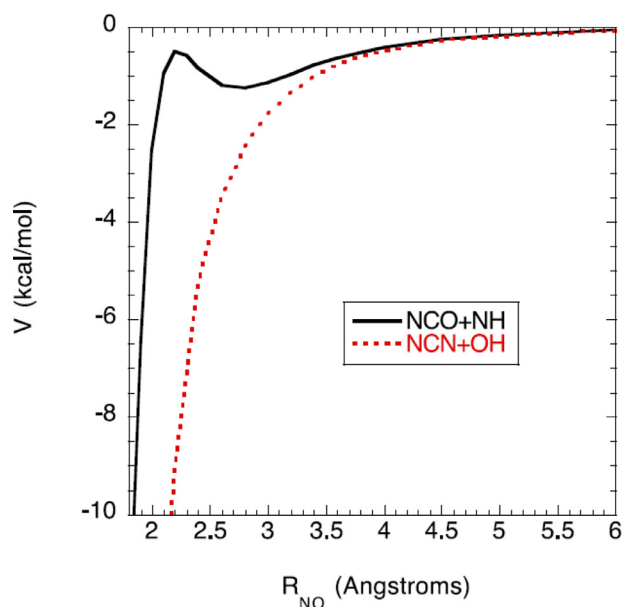


Fig. 9. Plot of the interaction energy for bringing two radicals together at fixed angle, and including a geometry relaxation correction.

For both channels we explored both (7e,7o) and (9e,8o) active spaces. For the NCN + OH channel the 7 active orbitals correlate with the π -space of NCN and the radical orbital of OH, while the extra orbital in the 8o case correlates with the lone-pair of OH. For the NCO + ³NH channel the 8 active orbitals correlate with the π -space of NCO and the two radical orbitals of NH. For the 7 active orbital case, the orbital correlating with the lone-pair of the O atom is removed from the active space. For the NCN + OH case, we found that the (7e,7o) space had improved convergence properties, while for the NCO + NH case the (9e,8o) space performed better.

Thus, the direct sampling in the VRC-TST analysis [79] was performed at the CASPT2(7e,7o)/cc-pVTZ level for NCN + OH and the CASPT2(9e,8o)/cc-pVTZ level for the NCO + NH case. Furthermore, for the NCO + NH case, we included the two nearly degenerate states in a two-state CAS wavefunction optimization and evaluated the energies of both states at the CASPT2 level, while for the NCN + OH case we simply evaluated the ground state at both the CAS and CASPT2 levels. These choices were made to facilitate convergence in the direct sampling. In addition to the direct sampling, we also incorporated one-dimensional corrections to account for the effects of geometry relaxation and to correct the minimum energy path to the spin-splitting evaluated average of the CASPT2 and MRCI+Q CBS limits. These one-dimensional corrections were evaluated for a range of fixed NO distances.

Qualitative minimum energy path (MEP) potentials for the two channels are illustrated in Fig. 9. These plots correspond to the calculated CASPT2/CBS interaction energies for variable separation at fixed approach angles that roughly correlate with the MEP. The fragments are held fixed with their asymptotic structure and a CASPT2/cc-pVTZ geometry relaxation correction is appended to the calculated interaction energy. The NCO + ³NH reaction shows a modest submerged barrier that arises because the dominant resonant form of NCO has the radical on the N end, whereas formation of NCONH requires that the radical be localized on the O end.

The NCN + OH channel would also show a submerged barrier, but at a larger separation of 3.0 Å (and the NCO + NH minimum would also be deeper), if the approach angle was optimized at each point along the MEP. Indeed, such long-range submerged barriers are ubiquitous in radical-radical reactions. They arise from the

transition from an orientation appropriate for chemical bonding (at short separations) to an orientation that maximizes long-range attractions (e.g., dipole-dipole or hydrogen bonding) at larger separations.

Predictions for the temperature and pressure dependence of the NCN + OH reaction kinetics were obtained from a master equation analysis employing the ANLO based ab initio TS theory estimates for each of the tight TSs and the VRC-TST fluxes for the NCN + OH and NCO + NH channels.

2.6.2. Results and discussion

The schematic potential energy surface illustrated in Fig. 8 shows significant differences from the corresponding plots from Zhu et al. [26]. Most importantly, we have discovered a new fully submerged pathway (black solid line) that ultimately connects the initial adduct with the products NCO + 3 NH. This pathway arises from a sequence with first an H transfer from NCNOH to NCNHO, followed by an O atom insertion that is accomplished through ring closure to form a three membered CNO ring and then ring opening to NCONH, and then finally ON bond fission to form the bimolecular products NCO + 3 NH. At low temperatures for low pressures this pathway should dominate the kinetics. At higher temperatures the relevance of this pathway will depend on the entropies of the TSs along this pathway relative to those for dissociation from some of the intermediates.

The largest energetic differences from the work of Zhu et al. arise for the decomposition to NCNO + H, which here is predicted to lie 4.3 kcal/mol higher in energy. Furthermore, we find that there is a reverse barrier of 3.2 kcal/mol, whereas Zhu et al. consider it to be barrierless. Taken together these differences effectively shut off the NCNO + H channel, making it largely irrelevant.

The maximum barrier along the pathway to HCN + NO lies at 5.5 kcal/mol. The TS entropy for the dissociation from NCNHO should be larger than that for the ring formation step in the NCN + NH forming pathway. Thus, this HCN + NO channel may compete effectively with that channel at higher temperatures.

The red dotted curve in Fig. 8 denotes a quartet state pathway, which may be of some significance at higher temperature as it involves solely atom addition and atom elimination channels whose TSs should be of relatively high entropy.

The present predictions for the temperature and pressure dependence of the phenomenological rate constants for the reaction of NCN with OH are illustrated in Figs. 10–12 for pressures of 0.01, 1, and 100 bar, respectively. At low pressures, bimolecular reactions dominate, with NCO + 3 NH the dominant channel at low temperature, while HCN + NO dominates at high temperature. We refrain here from making comparisons with the rate predictions of Zhu et al. [26]; with the abovementioned substantive differences in the potential energy surfaces there is little point in such comparisons.

At high pressures, stabilization dominates, with most of the flux stopping in the entrance adduct NCNOH. Notably, the NCNOH, NCNHO, and NCONH complexes are each thermodynamically stable until high temperatures and so should be included in chemical models. If observable, these three species could provide useful markers for the flux proceeding through NCN, and particularly through NCN + OH. The supplementary material contains modified Arrhenius fits to the rate constants for the phenomenological reactions from NCN + OH as well as from each of these three complexes. These fits are provided for temperatures ranging from 300 to 2500 K and for pressures ranging from 0.01 to 100 bar.

At intermediate pressures, stabilization dominates at low temperature, while bimolecular product formation dominates at high temperature. The key bimolecular products are again NCO + 3 NH and HCN + NO. The NCOH + 4 N and NCNO + H channels contribute at most 20% of the flux at all temperatures –and pressures examined here.

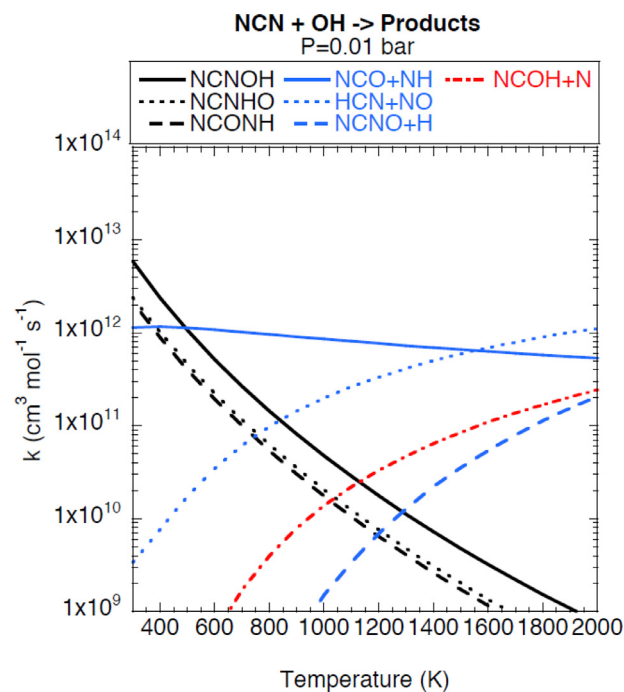


Fig. 10. Plot of the predicted rate constants for the NCN + OH reaction at a pressure of 0.01 bar. The black lines denote formation of stabilized unimolecular complexes, the blue lines denote bimolecular products formed through reaction on the doublet surface, and the red line denotes the bimolecular products of formed through reaction on the quartet surface. (For interpretation of the references to color in this figure legend, the reader is referred to the web version of this article.)

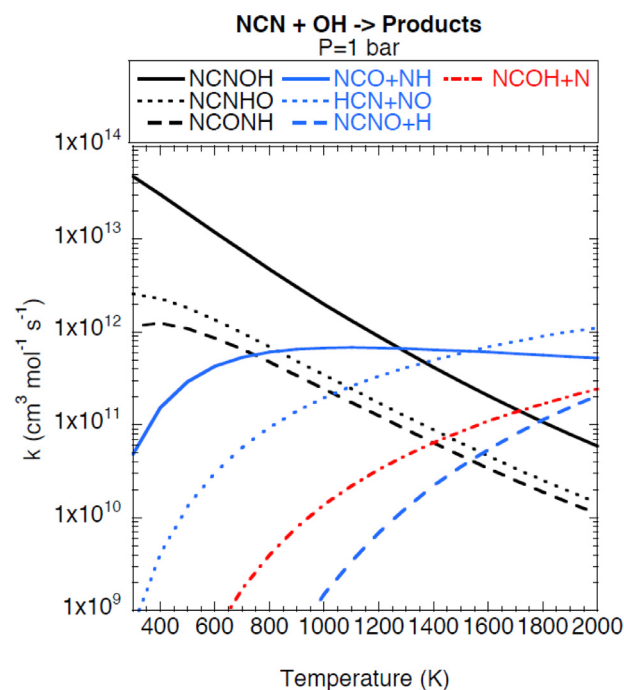


Fig. 11. Plot of the predicted rate constants for the NCN + OH reaction at a pressure of 1 bar. The black lines denote formation of stabilized unimolecular complexes, the blue lines denote bimolecular products formed through reaction on the doublet surface, and the red line denotes the bimolecular products of formed through reaction on the quartet surface. (For interpretation of the references to color in this figure legend, the reader is referred to the web version of this article.)

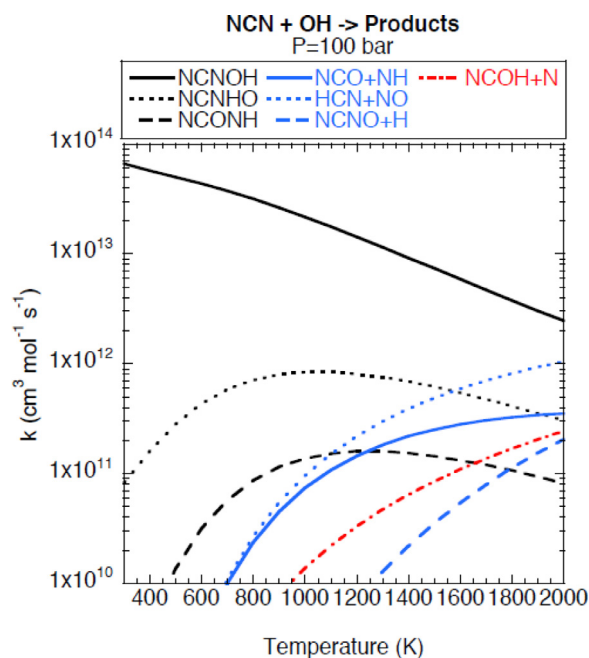


Fig. 12. Plot of the predicted rate constants for the $\text{NCN} + \text{OH}$ reaction at a pressure of 1 bar. The black lines denote formation of stabilized unimolecular complexes, the blue lines denote bimolecular products formed through reaction on the doublet surface, and the red line denotes the bimolecular products of formed through reaction on the quartet surface. (For interpretation of the references to color in this figure legend, the reader is referred to the web version of this article.)

3. Implications for modeling prompt NO formation at high pressure

The prompt NO mechanism is a major source of nitric oxide in combustion of gaseous fuels, in particular natural gas. Gas combustion typically takes place in stationary furnaces at atmospheric pressure or in engines and gas turbines at high pressure. Unfortunately, the knowledge of prompt NO formation at high pressure is limited. Most laboratory studies of the prompt NO mechanism have been conducted in laminar, premixed flames, typically at low pressure to increase the spatial resolution of the reaction zone [9–12,14,15,80]. Data obtained in premixed flames at higher pressure have been reported for a range of smaller hydrocarbons [32–37,39], but it is a challenge to characterize prompt NO formation under these conditions. The prompt NO mechanism is active in the reaction zone where hydrocarbon radicals may be formed in significant concentrations. However, at increased pressure the spatial resolution of the flame is low and there may be concerns about interaction with the burner surface if the flame is heavily stabilized. Interaction with the burner surface can be avoided by using an opposed-flow diffusion flame configuration. A number of high pressure studies have been reported for this flame configuration [40,41,43–45]. However, these results must also be interpreted cautiously because of the growing importance of other NO formation mechanisms with pressure. The enhanced fuel through-put at high pressure leads to increased flame temperatures, promoting thermal NO formation, while the pressure increase itself promotes NO formation through N_2O . In addition, the flow and mixing patterns facilitate removal of NO by reaction with hydrocarbon radicals. A further complication for both premixed and non-premixed flames is that LIF signals suffer from spectroscopic interferences at high pressure [81,82].

Despite these complications, the high-pressure flame studies have provided important information on the effect of pressure on

prompt NO formation. In premixed hydrocarbon flames, Laurendeau and coworkers [32,36] observed that with increasing pressure, the peak NO concentration shifted to leaner flames. They reported that the peaks in NO coincided with peaks in the maximum concentration of CH. If the measured NO levels are converted from the reported number densities [35] to mole fractions, it appears that NO, after an initial increase, decreases with increasing pressure above 6 atm in fuel-rich methane flames (see discussion below). Results from counter-flow diffusion flames fueled with methane show a similar behavior [41,43], with NO decreasing already above 3 atm and reaching small concentrations above 10 atm. Naik and coworkers [44,45,83] show that in the pressure range of 1–6 atm, the NO and CH concentrations are strongly correlated, both peaking at 2 atm and then decreasing with increasing pressure.

Modeling studies of prompt NO formation have been reported both for high-pressure premixed [34,37–40] and high-pressure counter-flow diffusion [41–45] flames. Most of these studies were conducted with the GRI-Mech mechanism (either version 2.11 or 3.0) or other mechanisms with $\text{CH} + \text{N}_2 \rightleftharpoons \text{HCN} + \text{H}$ as the initiation step; these mechanisms often failed to capture the observed pressure dependence for NO. Here, we re-evaluate the effect of pressure on prompt NO formation through chemical kinetic modeling, updating the prompt NO subset based on the theoretical results from the present work.

3.1. The chemical kinetic model

The chemical kinetic model used for the assessment of prompt NO formation at high pressure is largely drawn from the recent review by the authors on modeling of nitrogen chemistry in combustion [16]. The temperature and pressure dependent rate coefficients for $\text{CH} + \text{N}_2 \rightarrow \text{NCN} + \text{H}$ (R1), $\text{NCN} + \text{H} \rightarrow \text{products}$ (R2, R3), and $\text{NCN} + \text{OH} \rightarrow \text{products}$ (R4, R5) were adopted from the theoretical analysis in this work. Rate coefficients for the reactions on the HNCN and HONCN PES at selected pressures are listed in Table 5 and available in PLOG format together with the full mechanism as Supplemental Material.

At high pressure, the HNCN and HONCN adducts formed in reactions R1a, R2a, and R3a may stabilize. The oxidation chemistry of these species is not well established, but they would be expected to react rapidly with the O/H radical pool. Stabilization to cyc-NCHN, NCNHO, and NCONH would be expected to be of less importance under the conditions investigated below.

3.2. Results and discussion

The effect of pressure on the formation of prompt NO is investigated at different stoichiometries and temperatures through chemical kinetic modeling. The calculations were conducted with Chemkin PRO for a burner stabilized flame. We have chosen to compare predictions with the results from the laminar premixed $\text{CH}_4/\text{O}_2/\text{N}_2$ flames at pressures in the range 1.0–14.6 atm reported by Klassen et al. [35]. In Fig. 13, results are shown for NO as a function of pressure for three selected fuel-air equivalence ratios (0.8, 1.0, and 1.2). The measured data were obtained at a height of 0.7 cm above the burner surface for the lower pressures and at 0.3 cm for the highest pressures (presumably above 9 atm). Modeling predictions are shown for both locations.

The modeling is conducted assuming adiabatic conditions and solving the energy equation to obtain the flame temperature. As expected, the predicted temperatures are higher than indicated by measurements, but the difference is mostly within the experimental accuracy of ± 75 K [35]. The implication of overpredicting the temperature would be most pronounced in the lean and

Table 5

Selected reactions in the prompt NO mechanism subset. Parameters for use in the modified Arrhenius expression $k = AT^\beta \exp(-E/RT)$. Units are mol, cm, s, cal.

		A	β	E	Pressure	Source
1a.	$\text{CH} + \text{N}_2 \rightleftharpoons \text{HNCN}$	6.0E23	−4.41	14410	0.01 atm	pw
		1.4E23	−3.74	15820	1.0 atm	
		3.1E17	−1.78	15240	100 atm	
1b.	$\text{CH} + \text{N}_2 \rightleftharpoons \text{NCN} + \text{H}$	5.9E08	1.06	15960	0.01 atm	pw
		2.5E09	0.89	16620	1.0 atm	
		9.5E09	0.81	20340	100 atm	
2a.	$\text{NCN} + \text{H} \rightleftharpoons \text{HNCN}$	3.9E23	−4.34	5347	0.01 atm	pw
		1.5E30	−5.43	4415	1.0 atm	
		5.1E27	−4.15	5370	100 atm	
2b.	$\text{NCN} + \text{H} \rightleftharpoons \text{HCN} + \text{N}$	2.2E11	0.71	5321	0.01 atm	pw
		2.2E11	0.71	5321	1.0 atm	
		2.5E11	0.69	5371	100 atm	
2c.	$\text{NCN} + \text{H} \rightleftharpoons \text{HNC} + \text{N}$	3.9E−04	4.70	2440	0.01 atm	pw
		4.3E−04	4.69	2434	1.0 atm	
		9.6E−03	4.32	3641	100 atm	
3a.	$\text{NCN} + \text{OH} \rightleftharpoons \text{NCNOH}$	1.6E31	−6.65	2718	0.01 atm	pw
		1.8E32	−6.37	3924	1.0 atm	
		1.5E27	−4.35	3691	100 atm	
3b.	$\text{NCN} + \text{OH} \rightleftharpoons \text{HCN} + \text{NO}$	2.9E05	2.04	1505	0.01 atm	pw
		2.6E08	1.22	3593	1.0 atm	
		2.6E11	0.48	8655	100 atm	
3c.	$\text{NCN} + \text{OH} \rightleftharpoons \text{NCO} + \text{NH}$	8.6E14	−0.95	734	0.01 atm	pw
		1.7E18	−1.83	4143	1.0 atm	
		6.3E16	−1.25	10220	100 atm	
4.	$\text{NCN} + \text{H}_2 \rightleftharpoons \text{HNCN} + \text{H}$	4.1E13	0.00	24100		[22]
5a.	$\text{HNCN} + \text{O} \rightleftharpoons \text{HNC} + \text{NO}$	1.2E14	−0.05	72		[84]
5b.	$\text{HNCN} + \text{O} \rightleftharpoons \text{NH} + \text{NCO}$	5.6E13	−0.05	72		[84]
5c.	$\text{HNCN} + \text{O} \rightleftharpoons \text{CN} + \text{HNO}$	9.4E12	−0.05	72		[84]
6.	$\text{HNCN} + \text{OH} \rightleftharpoons \text{NCN} + \text{H}_2\text{O}$	1.0E05	2.48	−1887		[85]
7a.	$\text{NCNOH} \rightleftharpoons \text{NCO} + \text{NH}$	2.1E35	−7.73	56420	0.01 atm	pw
		5.8E36	−7.62	59640	1.0 atm	
		1.9E29	−4.97	62850	100 atm	
7b.	$\text{NCNOH} \rightleftharpoons \text{NCNO} + \text{H}$	9.9E−28	8.75	50680	0.01 atm	pw
		2.1E10	−1.12	66840	1.0 atm	
		9.2E26	−4.81	69960	100 atm	
7c.	$\text{NCNOH} \rightleftharpoons \text{HCN} + \text{NO}$	1.5E23	−4.81	52570	0.01 atm	pw
		4.2E30	−6.14	59260	1.0 atm	
		4.3E28	−4.78	62950	100 atm	
8a.	$\text{NCNOH} + \text{H} \rightleftharpoons \text{HNCN} + \text{OH}$	1.2E14	0.00	0		est
8b.	$\text{NCNOH} + \text{H} \rightleftharpoons \text{NH} + \text{CNOH}$	6.0E13	0.00	0		est
9a.	$\text{NCNOH} + \text{O} \rightleftharpoons \text{NCNO} + \text{OH}$	1.2E14	0.00	0		est
9b.	$\text{NCNOH} + \text{O} \rightleftharpoons \text{NO} + \text{CNOH}$	6.0E13	0.00	0		est
9c.	$\text{NCNOH} + \text{O} \rightleftharpoons \text{CN} + \text{HONO}$	6.0E13	0.00	0		est
10.	$\text{NCNOH} + \text{OH} \rightleftharpoons \text{NCNO} + \text{H}_2\text{O}$	6.0E13	0.00	0		est

stoichiometric flames where NO formation is most sensitive to temperature due to the contribution from thermal NO.

The results show that for the lean and stoichiometric flames, the NO concentration increases with pressure. The local peak in NO observed in these flames for a pressure of 6 atm is attributed to the change in measurement location from $\text{HAB} = 0.7$ cm (6 atm) to $\text{HAB} = 0.3$ cm (9 atm). The modeling predictions, which are in fairly good agreement with the experimental results, indicate that NO formation increases monotonically with pressure in these flames.

In the lean flames, NO is formed almost entirely from thermal NO and via the N_2O mechanism. The contribution from the N_2O scheme is most important early in the flame; when the temperature increases downstream, thermal NO is the dominant source of nitric oxide. This behavior is similar at low and high pressure. The enhanced NO formation at high pressure can mainly be attributed to a longer residence time at high temperature in the post-flame zone, even though a slight increase in temperature also contributes.

Under stoichiometric conditions, prompt NO formation dominates in the flame zone, accounting for 30–50% of the NO formed in the flame. Downstream of the reaction zone, thermal NO is the major source of NO. Again there is some contribution from the N_2O scheme, but it diminishes with increasing temperature in the post-

flame region. Similar to the lean flames, the increase in NO with increasing pressure is mainly related to NO formation in the post-flame, facilitated by a longer residence time as well as by a temperature increase of about 50 K from 1 atm to 6 atm.

For studying the effect of pressure on prompt NO formation, the rich flames with a fuel-air equivalence ratio of $\phi = 1.2$ are the most interesting. In these flames, almost all NO is formed from the prompt mechanism, independent of pressure. The experimental data show that the NO concentration initially increases with pressure, peaking at 6 atm, but then decreases with increasing pressure above this value. The modeling predictions are qualitatively in agreement with observations, except that the peak in NO is predicted already at a pressure of 3 atm. Both the measurements and the modeling predictions indicate that the flame temperature increases by about 50 K, when the pressure is raised from 1 to 6 atm and then levels out.

The prompt NO formation is initiated by attack of the CH radical on molecular nitrogen, mainly



In agreement with the results of Fig. 6, at high pressure the recombination reaction forming HNCN also contributes,



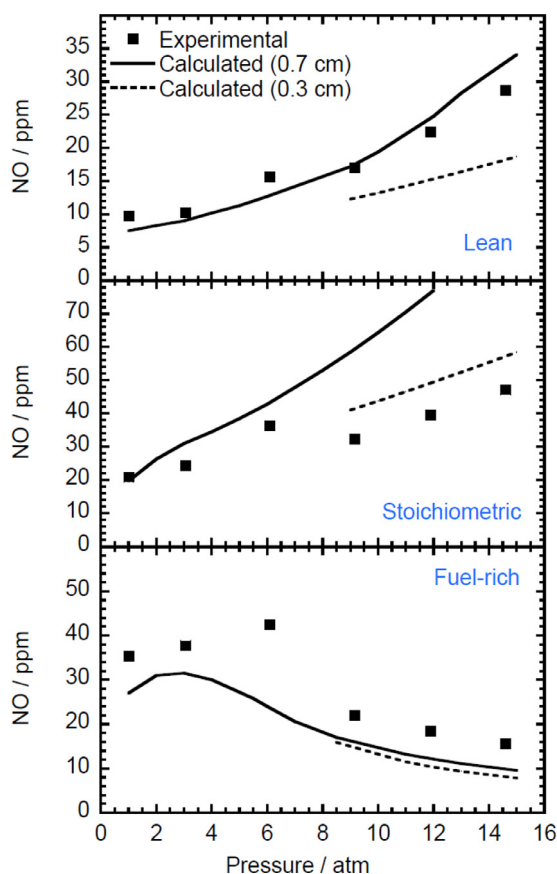


Fig. 13. Effect of pressure and fuel-air equivalence ratio on the formation of NO in premixed, laminar $\text{CH}_4/\text{O}_2/\text{N}_2$. The N_2/O_2 ratio of the oxidizer was 3.1. The fuel-air equivalence ratios are $\phi = 0.8$ (lean), 1.0 (stoichiometric) and 1.2 (fuel-rich). The experimental data, shown as symbols, are drawn from Klassen et al. [35]. Measurements of NO were conducted at 0.7 cm (1–6.1 atm.) and 0.3 cm (9.15–14.6 atm.) above the burner, respectively. Modeling predictions are shown as solid lines (HAB = 0.7 cm) and dashed lines (HAB = 0.3 cm).

According to the model, the NCN radical reacts mainly with atomic hydrogen in this rich flame,



Since atomic oxygen levels are low, the $\text{HCN} + \text{O}$ reaction proceeds slowly, and reaction R2b is followed mainly by the reaction sequence



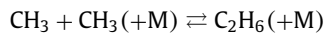
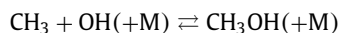
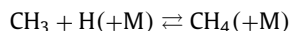
The pressure can affect the formation of prompt NO through temperature, total concentration, and residence time changes; through its impact on the fuel oxidation chemistry and formation of hydrocarbon radicals; and/or through its direct effect on the key reactions in the prompt NO scheme. The initial increase in NO with pressure can be attributed mainly to the increase in temperature in the flame zone. However, at pressures above 6 atm, the temperature levels out. Actually, it is conceivable that the temperature in the flame zone is even reduced at high pressures, since a heavier stabilization of the flame may lead to increased heat loss to the burner.

Under conditions of the fuel-rich flames in Fig. 13, the $\text{NCN} + \text{OH}$ reaction (R3) is not competitive and the prompt NO chemistry is dominated by reactions on the HNCN PES. Figs. 6 and 7 show the calculated pressure dependence for the individual product channels of the $\text{CH} + \text{N}_2$ (R1) and $\text{NCN} + \text{H}$ (R2) reactions. For $\text{CH} + \text{N}_2$ (R1), an increased pressure facilitates stabilization of HNCN (R1a) and reduces the formation of $\text{NCN} + \text{H}$ (R1b). However, HNCN

rapidly feeds into the cyanide and amine pool by reaction with radicals, and the change in product branching between (R1a) and (R1b) with pressure has little impact on the NO formation.

The impact of pressure on the product channels for $\text{NCN} + \text{H}$ (R2) was shown in Fig. 7. Stabilization of HNCN is insignificant at atmospheric pressure and below, but becomes important at high pressure. Predictions of prompt NO formation are sensitive to the yield of $\text{HCN} + \text{HNC}$ (promoting NO formation) compared to the yield of $\text{CH} + \text{N}_2$ (inhibiting NO formation). According to our theoretical calculations, the selectivity of $\text{NCN} + \text{H}$ for forming HCN and HNC does not appear to be a strong function of pressure, but the yield of $\text{CH} + \text{N}_2$ decreases strongly at high pressure. While this effect benefits NO formation, it is not sufficient to ensure an increase in prompt NO at elevated pressure.

The calculations indicate that the inhibiting effect of a high pressure on prompt NO can be attributed mostly to its impact on the radical pool. A high pressure promotes radical recombination reactions, such as



These chain terminating steps serve to reduce the peak concentrations of the O/H radicals by approximately an order of magnitude when the pressure is increased from 1 atm to 15 atm. The impact on the CH_n radical pool is even more pronounced, since the recombination reactions serve to weaken the formation of the smaller hydrocarbon radicals. According to the modeling predictions, the peak CH concentration is reduced by close to two orders of magnitude by this increase in pressure, strongly inhibiting prompt NO formation.

Modeling calculations were conducted also for a perfectly stirred reactor environment, partly because this configuration, characterized by short reaction times and high radical concentrations, favors formation of prompt NO [16], and partly because some of the complexities of the laminar flames discussed above are avoided. For clarity, we here decouple the impact of pressure and stoichiometry on the combustion temperature.

Figure 14 shows modeling predictions as a function of pressure and fuel-air equivalence ratio for formation of NO in combustion of methane under perfectly stirred reactor conditions. Predictions are shown for a temperature of 1800 K, which is sufficiently low to limit formation of thermal NO. The calculations are conducted for pressures of 0.01, 1.0, and 100 atm, both with the full mechanism (solid lines) and with a scheme where the prompt NO initiation reactions, i.e., $\text{CH} + \text{N}_2$ and $\text{C} + \text{N}_2$, were deactivated (dashed lines).

Prompt NO is seen to be the controlling NO formation mechanism under stoichiometric and reducing conditions. In line with the flame results, prompt NO formation is reduced when the pressure is increased from atmospheric to 10 atm. However, a further increase to 100 atm is seen to largely eliminate prompt NO formation. Again, the behavior can largely be attributed to the effect of pressure on the radical pool. At high pressure, the recombination reactions $\text{CH}_3 + \text{H}(+\text{M}) \rightarrow \text{CH}_4(+\text{M})$ and $\text{CH}_3 + \text{CH}_3(+\text{M}) \rightarrow \text{C}_2\text{H}_6(+\text{M})$ are responsible for a large part of the consumption of methyl radicals. Both reactions serve to weaken the formation of the smaller hydrocarbon radicals.

The dominating pathways in forming prompt NO change with pressure. At 1 and 10 atm, $\text{CH} + \text{N}_2 \rightarrow \text{NCN} + \text{H}$ is followed by reaction of NCN with H, O, and OH to form cyanides, amines and NO. With increasing pressure, also formation of HNCN from $\text{CH} + \text{N}_2$ and $\text{NCN} + \text{H}$ becomes important. At 100 atm, CH is

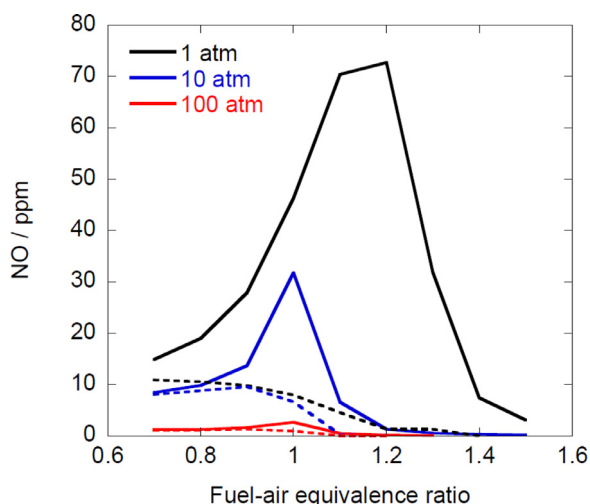


Fig. 14. The predicted effect of pressure and fuel-air equivalence ratio on the formation of NO in a perfectly stirred reactor, combusting a CH_4/air mixture. The temperature was 1800 K and the nominal residence time was 3 ms. The solid lines denote predictions with the full model, while calculations shown as dashed lines were conducted with the initiation reactions in prompt NO formation disabled.

almost depleted, with a concentration more than three orders of magnitude lower than at atmospheric pressure. Here, the reaction $\text{C} + \text{N}_2(+\text{M}) \rightarrow \text{NCN}(+\text{M})$ becomes the most important initiation step. The NCN radical then recombines with H to form HNCN, which feeds into the cyanide/amine pool by reaction with O/H radicals. Stabilization of HONCN contributes only at lower temperatures.

Our analysis indicates that while it is important to describe correctly the pressure dependence of the key reactions in prompt NO formation, the largest impact of pressure comes from its effect on the radical pool. Thereby the present analysis supports the findings of Naik and coworkers [44,45,83], who observed that in counter-flow diffusion flames the NO and CH concentrations were strongly correlated, both decreasing with increasing pressure above two atm.

4. Conclusions

High level theoretical methods have been employed to predict the heat of formation for NCN as well as the kinetics of the $\text{CH} + \text{N}_2$, $\text{H} + \text{NCN}$, and $\text{NCN} + \text{OH}$ reactions. The good agreement between the theoretically predicted heat of formation for NCN and the corresponding ATcT value indicates that the predictions are consistent with the available data. For the $\text{CH} + \text{N}_2$ and $\text{H} + \text{NCN}$ reactions the present high accuracy theoretical analyses provide a consistent (maximum discrepancies with experiment of about 30%) description of the literature data for both the forward and reverse reactions in the CHN_2 system. The analysis also predicts considerable stabilization to HNCN for both forward and reverse reactions at high pressure. For $\text{NCN} + \text{OH}$, the present analysis indicates the importance of a new pathway that yields $\text{NCO} + {}^3\text{NH}$. At high temperatures, the formation of $\text{NCO} + \text{NH}$ through this new pathway is predicted to be comparable to the formation of $\text{HCN} + \text{NO}$. At high pressures, significant stabilization to intermediate wells also occurs. These new predictions differ considerably from the earlier predictions of Zhu et al. [26].

The modeling simulations confirm that the pressure has an important impact on the prompt NO mechanism. For the rate determining step, $\text{CH} + \text{N}_2$ (R1), an increased pressure facilitates stabilization of HNCN (R1a) and reduces the formation of $\text{NCN} + \text{H}$ (R1b). According to our current predictions, this change in pathway

has only a limited impact on the NO formation rate, but more work on the HNCN reaction subset is desirable. Elevated pressures also promote radical recombination reactions, reducing concentrations of the radical pool and, in particular, of CH. This effect explains the observation from premixed and non-premixed flames that prompt NO formation decreases with increasing pressure above 2–3 atm.

Acknowledgments

Part of this material is based on work at Argonne supported by the U.S. Department of Energy, Office of Basic Energy Sciences, Division of Chemical Sciences, Geosciences, and Biosciences, under Contract No. DE-AC02-06CH11357 as part of the Argonne-Sandia Consortium on High-Pressure Combustion Chemistry, (ANL FWP # 59044). The work at DTU (P.G.) was financially supported by Innovation Fund Denmark.

Supplementary material

Supplementary material associated with this article can be found, in the online version, at [10.1016/j.combustflame.2018.04.029](https://doi.org/10.1016/j.combustflame.2018.04.029).

References

- [1] M.R. Roomina, R.W. Bilger, Conditional moment closure (CMC) predictions of a turbulent methane-air jet flame, *Combust. Flame* 125 (2001) 1176–1195.
- [2] C.P. Fenimore, Formation of nitric oxide in premixed hydrocarbon flames, *Symp. (Int.) Combust.* 13 (1971) 373–380.
- [3] A.N. Hayhurst, I.M. Vince, Nitric-oxide formation from N_2 in flames - the importance of prompt NO, *Prog. Energy Combust. Sci.* 6 (1980) 35–51.
- [4] P. Glarborg, J.A. Miller, R.J. Kee, Kinetic modeling and sensitivity analysis of nitrogen oxide formation in well-stirred reactors, *Combust. Flame* 65 (1986) 177–202.
- [5] J.A. Miller, C.T. Bowman, Mechanism and modeling of nitrogen chemistry in combustion, *Prog. Energy Combust. Sci.* 15 (1989) 287–338.
- [6] J.A. Miller, S.P. Walch, Prompt NO: Theoretical prediction of the high-temperature rate coefficient for $\text{CH} + \text{N}_2 \rightarrow \text{HCN} + \text{N}$, *Int. J. Chem. Kinet.* 29 (1997) 253.
- [7] L. Cui, K. Morokuma, J.M. Bowman, S.J. Klippenstein, The spin-forbidden reaction $\text{CH} + \text{N}_2 \rightarrow \text{HCN} + \text{N}$ revisited. II. Nonadiabatic transition state theory and application, *J. Chem. Phys.* 110 (1999) 9469–9482.
- [8] L.V. Moskaleva, M.C. Lin, The spin-conserved reaction $\text{CH} + \text{N}_2 \rightarrow \text{H} + \text{NCN}$: A major pathway to prompt NO studied by quantum/statistical theory calculations and kinetic modeling of rate constant, *Proc. Combust. Inst.* 28 (2000) 2393–2401.
- [9] N. Lamoureux, X. Mercier, C. Western, J.F. Pauwels, P. Desgroux, NCN quantitative measurement in a laminar low pressure flame, *Proc. Combust. Inst.* 32 (2009) 937–944.
- [10] N. Lamoureux, P. Desgroux, A.E. Bakali, J.F. Pauwels, Experimental and numerical study of the role of NCN in prompt-NO formation in low-pressure $\text{CH}_4\text{-O}_2\text{-N}_2$ and $\text{C}_2\text{H}_2\text{-O}_2\text{-N}_2$ flames, *Combust. Flame* 157 (2010) 1929–1941.
- [11] N. Lamoureux, P. Desgroux, A.E. Bakali, J.F. Pauwels, Experimental and numerical study of the role of NCN in the prompt-NO formation in low pressure $\text{CH}_4/\text{O}_2/\text{N}_2$ and $\text{C}_2\text{H}_2/\text{O}_2/\text{N}_2$ flames, *Combust. Flame* 160 (2013) 745–746.
- [12] N. Lamoureux, C.M. Western, X. Mercier, P. Desgroux, Reinvestigation of the spectroscopy of the $\text{A}^3\Pi_u\text{-X}^3\Sigma_g^-\text{transition}$ of the NCN radical at high temperature: application to quantitative NCN measurement in flames, *Combust. Flame* 160 (2013) 755–765.
- [13] N. Lamoureux, H.E. Merhubi, X. Mercier, J.F. Pauwels, P. Desgroux, HCN quantitative measurement in a laminar low pressure flame at 1036 nm using pulsed CRDS technique, *Proc. Combust. Inst.* 34 (2013) 3557–3564.
- [14] N. Lamoureux, H.E. Merhubi, L. Gasnot, C. Schoenmaecker, P. Desgroux, Measurements and modelling of HCN and CN species profiles in laminar $\text{CH}_4/\text{O}_2/\text{N}_2$ low pressure flames using LIF/CRDS techniques, *Proc. Combust. Inst.* 35 (2015) 745–752.
- [15] N. Lamoureux, H.E. Merhubi, L. Pillier, S. de Persis, P. Desgroux, Modeling of NO formation in low pressure premixed flames, *Combust. Flame* 163 (2016) 557–575.
- [16] P. Glarborg, J.A. Miller, B. Ruscic, S.J. Klippenstein, Modeling nitrogen chemistry in combustion, *Prog. Energy Combust. Sci.* 67 (2018) 31–68.
- [17] A.J. Dean, R.K. Hanson, C.T. Bowman, High temperature shock tube study of reactions of CH and C-atoms with N_2 , *Symp. (Int.) Combust.* 23 (1991) 259–265.
- [18] V. Vasudevan, R.K. Hanson, C.T. Bowman, D.M. Golden, D.F. Davidson, Shock tube study of the reaction of CH with N_2 : overall rate and branching ratio, *J. Phys. Chem. A* 111 (2007) 11818–11830.
- [19] L.B. Harding, S.J. Klippenstein, J.A. Miller, Kinetics of $\text{CH} + \text{N}_2$ revisited with multireference methods, *J. Phys. Chem. A* 112 (2008) 522–532.

- [20] W.-S. Teng, L.V. Moskaleva, H.-L. Chen, M.C. Lin, Ab initio chemical kinetics for H + NCN: Prediction of NCN heat of formation and reaction product branching via doublet and quartet surfaces, *J. Phys. Chem. A* 117 (2013) 5775–5784.
- [21] J. Dammeier, N. Faßheber, G. Friedrichs, Direct measurements of the high temperature rate constants of the reactions $\text{NCN} + \text{O}$, $\text{NCN} + \text{NCN}$, and $\text{NCN} + \text{M}$, *Phys. Chem. Chem. Phys.* 14 (2012) 1030–1037.
- [22] N. Faßheber, J. Dammeier, G. Friedrichs, Direct measurements of the total rate constant of the reaction $\text{NCN} + \text{H}$ and implications for the product branching ratio and the enthalpy of formation of NCN, *Phys. Chem. Chem. Phys.* 16 (2014) 11647–11657.
- [23] N. Faßheber, G. Friedrichs, Shock tube measurements of the rate constant of the reaction $\text{NCN} + \text{O}_2$, *Int. J. Chem. Kinet.* 47 (2015) 586–595.
- [24] J. Dammeier, G. Friedrichs, Direct measurements of the rate constants of the reactions $\text{NCN} + \text{NO}$ and $\text{NCN} + \text{NO}_2$ behind shock waves, *J. Phys. Chem. A* 115 (2011) 14382–14390.
- [25] R.S. Zhu, M.C. Lin, Ab initio study on the oxidation of NCN by O: Prediction of the total rate constant and product branching ratios, *J. Phys. Chem. A* 111 (2007) 6766–6771.
- [26] R.S. Zhu, H.M.T. Nguyen, M.C. Lin, Ab initio study on the oxidation of NCN by OH: prediction of the individual and total rate constants, *J. Phys. Chem. A* 113 (2009) 298–304.
- [27] R.S. Zhu, M.C. Lin, Ab initio study of the oxidation of NCN by O_2 , *Int. J. Chem. Kinet.* 37 (2005) 593–598.
- [28] J. Hetzler, M. Olzmann, Collisional relaxation of NCN: An experimental study with laser-induced fluorescence, *Z. Phys. Chem.* 229 (2015) 1503–1519.
- [29] A. Busch, N. Gonzalez-Garcia, G. Lendvay, M. Olzmann, Thermal decomposition of NCN: Shock-tube study, quantum chemical calculations, and master-equation modeling, *J. Phys. Chem. A* 119 (2015) 7838–7846.
- [30] O. Welz, M. Olzmann, Kinetics of the $\text{NCN} + \text{NO}$ reaction over a broad temperature and pressure range, *J. Phys. Chem. A* 116 (2012) 7293–7301.
- [31] E. Goos, C. Sickfeld, F. Mauss, L. Seidel, B. Ruscic, A. Burcat, T. Zeuch, Prompt NO formation in flames: The influence of NCN thermochemistry, *Proc. Combust. Inst.* 34 (2013) 657–666.
- [32] J.R. Reisel, C.D. Carter, N.M. Laurendeau, Laser-induced fluorescence measurements of nitric-oxide in laminar $\text{C}_2\text{H}_6/\text{O}_2/\text{N}_2$ flames at high-pressure, *Combust. Flame* 92 (1993) 485–489.
- [33] J.R. Reisel, N.M. Laurendeau, Laser-induced fluorescence measurements and modeling of nitric-oxide formation in high-pressure flames, *Combust. Sci. Technol.* 98 (1994) 137–160.
- [34] J.R. Reisel, N.M. Laurendeau, Quantitative LIF measurements and modeling of nitric-oxide in high-pressure $\text{C}_2\text{H}_4/\text{O}_2/\text{N}_2$ flames, *Combust. Flame* 101 (1995) 141–152.
- [35] M.S. Klassen, D.D. Thomsen, J.R. Reisel, N.M. Laurendeau, Laser-induced fluorescence measurements of nitric oxide formation in high-pressure premixed methane flames, *Combust. Sci. Technol.* 111 (1995) 229–247.
- [36] D.D. Thomsen, F.F. Kuligowski, N.M. Laurendeau, Background corrections for laser-induced-fluorescence measurements of nitric oxide in lean, high-pressure, premixed methane flames, *Appl. Optics* 36 (1997) 3244–3252.
- [37] D.D. Thomsen, F.F. Kuligowski, N.M. Laurendeau, Modeling of NO formation in premixed, high-pressure methane flames, *Combust. Flame* 119 (1999) 307–318.
- [38] J.R. Reisel, Modeling of nitric oxide formation in high-pressure premixed laminar ethane flames, *Combust. Flame* 120 (2000) 233–241.
- [39] D. Charlston-Goch, B.L. Chadwick, R.J.S. Morrison, A. Campisi, D.D. Thomsen, N.M. Laurendeau, Laser-induced fluorescence measurements and modeling of nitric oxide in premixed flames of $\text{CO} + \text{H}_2 + \text{CH}_4$ and air at high pressures I. Nitrogen fixation, *Combust. Flame* 125 (2001) 729–743.
- [40] L. Pillier, M. Idir, J. Molet, A. Matynia, S. de Persis, Experimental study and modelling of NOx formation in high pressure counter-flow premixed CH_4/air flames, *Fuel* 150 (2015) 394–407.
- [41] R.V. Ravikrishna, D.D. Thomsen, N.M. Laurendeau, Laser-induced fluorescence measurements and modeling of nitric oxide in high-pressure counterflow diffusion flames, *Combust. Sci. Technol.* 157 (2000) 243–261.
- [42] C.H. Sohn, I.M. Jeong, S.H. Chung, Numerical study of the effects of pressure and air-dilution on NO formation in laminar counterflow diffusion flames of methane in high temperature air, *Combust. Flame* 130 (2002) 83–93.
- [43] R.V. Ravikrishna, S.V. Naik, C.S. Cooper, N.M. Laurendeau, Quantitative laser-induced fluorescence measurements and modeling of nitric oxide in high-pressure (6–15 atm) counterflow diffusion flames, *Combust. Sci. Technol.* 176 (2004) 1–21.
- [44] S.V. Naik, N.M. Laurendeau, LIF measurements and chemical kinetic analysis of nitric oxide formation in high-pressure counterflow partially premixed and nonpremixed flames, *Combust. Sci. Technol.* 176 (2004) 1809–1853.
- [45] S.V. Naik, N.A. Laurendeau, Effects of CH-NO interactions on kinetics of prompt NO in high-pressure counterflow flames, *Energy Fuels* 22 (2008) 250–261.
- [46] K.A. Peterson, D. Feller, D.A. Dixon, Chemical accuracy in ab initio thermochemistry and spectroscopy: Current strategies and future challenges, *Theor. Chem. Acc.* 131 (2012) 1079–1099.
- [47] L.B. Harding, S.J. Klippenstein, A.W. Jasper, Ab initio methods for reactive potential surfaces, *Phys. Chem. Chem. Phys.* 9 (2007) 4055–4070.
- [48] J.D. Watts, J. Gauss, R.J. Bartlett, Coupled-cluster methods with noniterative triple excitations for restricted open-shell Hartree-Fock and other general single determinant reference functions energies and analytical gradients, *J. Chem. Phys.* 98 (1993) 8718–8733.
- [49] S.J. Klippenstein, L.B. Harding, B. Ruscic, Ab initio computations and active thermochemical tables hand in hand: Heats of formation of core combustion species, *J. Phys. Chem. A* 121 (2017) 6580–6602.
- [50] S.R. Langhoff, E.R. Davidson, Configuration interaction calculations on nitrogen molecule, *Int. J. Quantum Chem.* 8 (1974) 61–72.
- [51] C.F. Goldsmith, L.B. Harding, Y. Georgievskii, J.A. Miller, S.J. Klippenstein, Temperature and pressure dependent rate coefficients for the reaction of vinyl radical with molecular oxygen, *J. Phys. Chem. A* 119 (2015) 7766–7779.
- [52] D.G. Truhlar, B.C. Garrett, S.J. Klippenstein, Current status of transition state theory, *J. Phys. Chem.* 100 (1996) 12771–12800.
- [53] J.A. Miller, S.J. Klippenstein, Master equation methods in gas phase chemical kinetics, *J. Phys. Chem. A* 110 (2006) 10528–10544.
- [54] Y. Georgievskii, J.A. Miller, M.P. Burke, S.J. Klippenstein, Reformulation and solution of the master equation for multiple-well chemical reactions, *J. Phys. Chem. A* 117 (2013) 12146–12154.
- [55] Y. Feng, J.T. Niiranen, A. Bencsura, V.D. Knyazev, D. Gutman, W. Tsang, Weak collision effects in the reaction $\text{C}_2\text{H}_5 = \text{C}_2\text{H}_4 + \text{H}$, *J. Phys. Chem.* 87 (1993) 871–880.
- [56] A.W. Jasper, J.A. Miller, Collisional energy transfer in unimolecular reactions: Direct classical trajectories for $\text{CH}_4 = \text{CH}_3 + \text{H}$ in helium, *J. Phys. Chem. A* 113 (2009) 5612–5619.
- [57] S.J. Klippenstein, From theoretical reaction dynamics to chemical modeling of combustion, *Proc. Comb. Inst.* 36 (2017) 77–111.
- [58] Y. Georgievskii, S.J. Klippenstein, Transition state theory for multichannel addition reactions: Multifaceted dividing surfaces, *J. Phys. Chem. A* 107 (2003) 9776–9781.
- [59] L.B. Harding, Y. Georgievskii, S.J. Klippenstein, Predictive theory for hydrogen atom – hydrocarbon radical association kinetics, *J. Phys. Chem. A* 109 (2005) 4646–4656.
- [60] S.J. Klippenstein, Y. Georgievskii, L.B. Harding, Predictive theory for the combination kinetics of two alkyl radicals, *Phys. Chem. Chem. Phys.* 8 (2006) 1133–1147.
- [61] H.-J. Werner, P.J. Knowles, G. Knizia, M. Schutz, P. Celani, T. Korona, R. Lindh, A. Mitrushenkov, G. Rauhut, K.R. Shamasundar, T.B. Adler, R.D. Amos, A. Bernhardsson, A. Berning, D.L. Cooper, M.J.O. Deegan, A.J. Dobbyn, F. Eckert, E. Goll, C. Hampel, A. Hesselmann, T.H. G. Hetzer, G. Jansen, C. Koppl, Y. Liu, A.W. Lloyd, R.A. Mata, A.J. May, S.J. McNicholas, W. Meyer, M.E. Mura, A. Nicklass, D.P. O'Neill, P. Palmieri, D. Peng, K. Pflüger, R. Pitzer, M. Reiher, T. Shiozaki, H. Stoll, A.J. Stone, R. Tarroni, T. Thorsteinsson, M. Wang, MOLPRO, version 2012.1, a package of ab initio programs (2012). Cardiff, UK
- [62] J.F. Stanton, J. Gauss, M.E. Harding, P.G. Szalay, with contributions from Auer, A. A.; Bartlett, R. J.; Benedikt, U.; Berger, C.; Bernholdt, D. E.; Bomble, Y. J.; et al., and the integral packages MOLECULE (Almlöf, J.; Taylor, P. R.), PROPS (Taylor, P. R.), ABACUS (Helgaker, T.; Jensen, H. J.; Jorgensen, P.; Olsen, J.), and ECP routines by Mitin, A. V.; van Wullen, C. For the current version, see: <http://www.cfour.de>, 2010.
- [63] M. Kallay, MRCC, A string-based quantum chemical program Suite. See also M. Kallay, P.R. Surjan, Higher excitations in coupled-cluster theory, *J. Chem. Phys.* 115 (2001) 2945–2954.
- [64] M.J. Frisch, G.W. Trucks, H.B. Schlegel, G.E. Scuseria, M.A. Robb, J.R. Cheeseman, G. Scalmani, V. Barone, B. Mennucci, G.A. Petersson, et al., Gaussian 09, Revision D.01, Gaussian, Inc., Wallingford CT (2009).
- [65] Y. Georgievskii, L.B. Harding, S.J. Klippenstein, VaReCoF. 2017.5.19, <http://tcg.cse.anl.gov/papr/codes/VaReCoF.html>, Argonne National Laboratory, 2017.
- [66] Y. Georgievskii, S.J. Klippenstein, MESS.2016.3.23, Argonne National Laboratory (2016). <http://tcg.cse.anl.gov/papr/codes/mess.html>
- [67] M. Pfeifle, A. Jasper, NST: A simple minimum-on-the-seam-of-crossings (MSX) optimizer and nonadiabatic statistical theory (NST) flux calculator (2016). <http://tcg.cse.anl.gov/papr/codes/nst.html>, Sandia and Argonne National Laboratories
- [68] D.E. Milligan, M.E. Jacox, A.M. Bass, Matrix-isolation study of the photolysis of cyanogen azide. The infrared and ultraviolet spectra of the free radical NCN, *J. Phys. Chem.* 43 (1966) 3149–3160.
- [69] D.E. Milligan, M.E. Jacox, Matrix-isolation study of the photolysis of cyanogen azide. II. The symmetric stretching fundamental of the free radical NCN, *J. Phys. Chem.* 45 (1966) 1387–1391.
- [70] M. Pfeifle, Y. Georgievskii, A.W. Jasper, S.J. Klippenstein, Theoretical investigation of intersystem crossing in the cyanonitrene molecules $^1\text{NCN} \rightarrow ^3\text{NCN}$, *J. Chem. Phys.* 147 (2017) 084310.
- [71] J.C. Lorquet, B. Leyh-Nihant, Nonadiabatic unimolecular reactions. 1. A statistical formulation for the rate constants, *J. Phys. Chem.* 92 (1988) 4778–4783.
- [72] J.N. Harvey, Understanding the kinetics of spin-forbidden chemical reactions, *Phys. Chem. Chem. Phys.* 9 (2007) 331–343.
- [73] A.W. Jasper, Multidimensional effects in nonadiabatic statistical theories of spin-forbidden kinetics: A case study of $^3\text{O} + \text{CO} \rightarrow \text{CO}_2$, *J. Phys. Chem. A* 119 (2015) 7339–7351.
- [74] P.J. Knowles, H.-J. Werner, An efficient method of the evaluation of coupling-coefficients in configuration-interaction calculations, *Chem. Phys. Lett.* 145 (1988) 514–522.
- [75] P.J. Knowles, H.-J. Werner, Internally contracted multiconfiguration-reference configuration-interaction calculations for excited-states, *Theor. Chim. Acta* 84 (1992) 95–103.
- [76] H.J. Werner, P.J. Knowles, An efficient internally contracted multiconfiguration reference configuration-interaction method, *J. Chem. Phys.* 89 (1988) 5803–5814.
- [77] N. Koga, K. Morokuma, Determination of the lowest energy point on the crossing seam between 2 potential surfaces using the energy gradient, *Chem. Phys. Lett.* 119 (1985) 371–374.

- [78] J.B. Delos, W.R. Thorson, Studies of the potential-curve-crossing problem. II. General theory and a model for close crossings, *Phys. Rev. A* 6 (1972) 728–745.
- [79] S.J. Klippenstein, Variational optimizations in RRKM theory calculations for unimolecular dissociation reactions with no reverse barrier, *J. Phys. Chem.* 96 (1992) 367–371.
- [80] P.A. Berg, D.A. Hill, A.R. Noble, G.P. Smith, J.B. Jeffries, D.R. Crosley, Absolute CH concentration measurements in low-pressure methane flames: Comparisons with model results, *Combust. Flame* 121 (2000) 223–235.
- [81] C. Schulz, V. Sick, U.E. Meier, J. Heinze, W. Stricker, Quantification of NO A-X(0,2) laser-induced fluorescence: Investigation of calibration and collisional influences in high-pressure flames, *Appl. Opt.* 38 (1999) 1434–1443.
- [82] W.G. Bessler, C. Schulz, T. Lee, J.B. Jeffries, R.K. Hanson, Strategies for laser-induced fluorescence detection of nitric oxide in high-pressure flames. I. A-X(0,0) excitation, *Appl. Opt.* 41 (2002) 3547–3557.
- [83] S.V. Naik, N.M. Laurendeau, LIF measurements and chemical kinetic analysis of methylidyne formation in high-pressure counter-flow partially premixed and non-premixed flames, *Appl. Phys. B: Laser Opt.* 79 (2004) 891–905.
- [84] S. Xu, M.C. Lin, Ab initio chemical kinetics for the reactions of HNCN with O(³P) and O₂, *Proc. Combust. Inst.* 32 (2009) 99–106.
- [85] S. Xu, M.C. Lin, Ab initio chemical kinetics for the OH + HNCN reaction, *J. Phys. Chem. A* 111 (2007) 6730–6740.